

NOTICE

**CERTAIN DATA
CONTAINED IN THIS
DOCUMENT MAY BE
DIFFICULT TO READ
IN MICROFICHE
PRODUCTS.**

LA-UR 91 - 532

Conf-9011267-

11-11-90

Los Alamos National Laboratory is operated by the University of California for the United States Department of Energy under contract W-7405-ENG-36

LA-UR--91-532

DE91 008587

TITLE ADVANCED, TIME-RESOLVED IMAGING TECHNIQUES
FOR ELECTRON-BEAM CHARACTERIZATIONS

AUTHOR(S) Alex H. Lumpkin

SUBMITTED TO Proceedings of the Workshop on Accelerator Instrumentation,
Fermi National Accelerator Laboratory, Batavia, Illinois
October 1-4, 1990

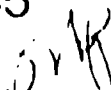
DISCLAIMER

This report was prepared as an account of work sponsored by an agency of the United States Government. Neither the United States Government nor any agency thereof, nor any of their employees, makes any warranty, express or implied, or assumes any legal liability or responsibility for the accuracy, completeness, or usefulness of any information, apparatus, product, or process disclosed, or represents that its use would not infringe privately owned rights. Reference herein to any specific commercial product, process, or service by trade name, trademark, manufacturer, or otherwise does not necessarily constitute or imply its endorsement, recommendation, or favoring by the United States Government or any agency thereof. The views and opinions of authors expressed herein do not necessarily state or reflect those of the United States Government or any agency thereof.

By acceptance of this article, the publisher recognizes that the U.S. Government retains a nonexclusive, royalty-free license to publish or reproduce the published form of this contribution, or to allow others to do so, for U.S. Government purposes.

The Los Alamos National Laboratory requests that the publisher identify this article as work performed under the auspices of the U.S. Department of Energy.

 **Los Alamos** Los Alamos National Laboratory
Los Alamos, New Mexico 87545

DISTRIBUTION OF THIS DOCUMENT IS UNLIMITED. 

ADVANCED, TIME-RESOLVED IMAGING TECHNIQUES
FOR ELECTRON-BEAM CHARACTERIZATIONS*

Alex H. Lumpkin
Physics Division, Los Alamos National Laboratory
Los Alamos, New Mexico 87545

ABSTRACT

Several unique time-resolved imaging techniques have been developed to address radio frequency (RF)-linac generated electron beams and the free-electron lasers (FEL) driven by such systems. The time structures of these beams involve a series of micropulses with 10 to 15-ps duration, separated by tens of nanoseconds. Mechanisms to convert the e-beam information to optical radiation include optical transition radiation (OTR), Cherenkov radiation, spontaneous emission radiation (SER), and the FEL mechanism itself. The use of gated, intensified television cameras and synchroscan and dual-sweep streak cameras to time-resolve these signals has greatly enhanced the power of these techniques. A brief review of the less familiar conversion mechanisms and electro-optic techniques is followed by a series of specific experimental examples from the RF linac FEL facilities at Los Alamos and Boeing (Seattle, WA).

I. INTRODUCTION

Using advanced, electro-optic imaging principles, several time-resolved diagnostic techniques have been adapted to the characterization of electron beams accelerated by radio frequency (RF) linear accelerator (Linac) structures to drive free-electron lasers (FEL).¹⁻³ Both submicropulse (10 ps) and submacropulse (100 μ s) effects have been addressed. The e-beam information can be converted to optical radiation in the visible regime by the optical transition radiation (OTR), Cherenkov (CH), synchrotron radiation (SR), spontaneous emission radiation (SER), or even the FEL mechanisms. Besides gated, intensified cameras we have used streak cameras operating in the fast, slow, synchroscan, and dual-sweep modes.⁴⁻⁶ The latter two modes have been shown to be particularly useful for understanding RF-linac related systems due to the relatively low jitter of the phase-locked synchroscan unit when compared with a 10-ps pulse or to the jitter of a single, fast streak sweep.

It should be pointed out that these techniques have been developed within the Los Alamos FEL program and were optimized for such systems. One recalls that the FEL simply consists of the RF-

*Work supported and funded by the U.S. Department of Defense, Army Strategic Defense Command, under the auspices of the U.S. Department of Energy.

linac, the wiggler, and the resonator cavity as shown in Fig. 1.⁷ Also, to obtain FEL signal buildup, a series of electron pulses is brought to the wiggler at a spacing equal to the round trip transit time in the cavity. This results in somewhat specialized pulse trains (macropulse) composed of many micropulses as schematically shown in Fig. 2. This time structure then dictates the diagnostic requirements.

II. ELECTRON-BEAM PARAMETERS AND DIAGNOSTIC TECHNIQUES

In this section, an outline of the various e-beam parameters that can be addressed and the particular electro-optic techniques that have been demonstrated within our RF-linac driven FEL programs will be described.

Beam Parameters

Most of this work has been done via my involvement in programs on the Los Alamos FEL facility (~20 MeV linac) or the Boeing visible FEL facility (~110 MeV linac). As an example, Fig. 3 shows a schematic of the High Brightness Accelerator FEL (HIBAF) Facility diagnostics at Los Alamos.⁶ After the linac (only two accelerators at this point) a series of beam position and profile screen (aluminized fused silica), stations (0-3) are included along the beam line before and after the quadrupole. Each was viewed by an intensified television camera [either silicon intensified target (SIT) or gated, intensified charge-injection-device (ICID)]. The sensitivity of these cameras was such as to image via OTR a single e-beam micropulse of about 3 to 5 nC charge and 15-17 MeV in energy. All screens used were designed for OTR experiments except the fourth station where a 45° port also provided Cherenkov radiation imaging. The beamline was terminated with a 90° spectrometer and beam dump whose focal plane had a fused-silica screen to generate Cherenkov light. This scene was imaged by two other intensified cameras. The parameters investigated are shown in Table I and include beam position, beam profile, divergence, emittance, pointing, charge, energy (spread, jitter, slew), micropulse duration, drive laser micropulse duration (jitter and slew), and beam spill. The table provides the nominal value, its span, the technique, estimated resolution error and timescale. All but the charge and beam spill were directly assessed via imaging techniques. Recalling our pulse structure of a series of micropulses of 10 to 15 ps duration separated by 46 ns over about 100 μ s, the last column addresses whether the time-resolved information separates the individual micropulses (submacropulse) or resolves information within the micropulse (i.e., submicropulse).

Diagnostic Techniques

There are two aspects to these imaging techniques that bear attention. The first involves the necessity of converting the electron-beam parameter information into optical (generally, visible) radiation that can be detected by these electro-optic devices. Mechanisms that have been employed include OTR, CH, SER, SR, and the FEL itself. Additionally, the photoelectric injector (PEI) at HIBAF is driven by a ND:YLF oscillator, which has been frequently doubled into the green at 527 nm. This wavelength is directly detectable with our techniques. The second aspect involves the rather novel application of streak/spectrometers, synchroscan, and dual-sweep streak techniques that have been applied to the imaging problems and are somewhat unique to our programs.

Conversion Mechanisms

Our motivations for exploring OTR techniques include the following:

1. Most relevant e-beam parameters measurable at a single axial location,
2. Need for better spatial resolution on beam profile (100 μm or better),
3. Need for on-line emittance measurement,
4. Improved emittance expected with photoelectric injector,
5. Competition of sources with fused silica plus metal mirror geometry,
6. Technique for future beam profile, intensity, pointing, emittance, energy,
7. Reduced beam scattering and x-rays, and
8. Wiggler diagnostics position and angle.

OTR was first predicted by Ginzburg and Frank in 1946,⁸ but its practical usefulness as an e-beam diagnostic was not explored or demonstrated until 1975 by Wartski⁹ with further development in the 1980s by Fiorito and Rule.^{10,11} The first demonstrations of applications to the actual linacs driving FELs has been reported by Lumpkin, et al.^{12,13} and they are part of our discussion here. OTR is generated when a charged particle beam crosses the interface, or transition, between two media of different dielectric constants. This means that the effective spatial resolution limit in diagnostics becomes the optical sensor, and one is no longer limited by the thickness of the fused silica or phosphor. In a poster paper at this Workshop, Rule and Fiorito discuss the micron-resolution imaging potential.¹⁴ The OTR angular distribution pattern can be exploited to measure e-beam divergence and energy, although these two parameters are somewhat convoluted. One of its more useful features is that the backward lobes of

radiation are emitted around the angle of specular reflection so that a foil at 45° to the beam emits at 90° to the beam, a standard port geometry for accelerator beam lines (see Fig. 4). An approximate expression for the angular distribution from a single foil given by Wartski⁹ for high γ and $|\epsilon| > 1$ is:

$$\frac{d^2W}{d\omega d\Omega} \approx \frac{e^2}{\pi^2 c} \cdot \frac{\theta^2}{(\theta^2 + \gamma^{-2})^2} \times F(\psi, \theta, \omega) \quad (1)$$

θ is angle with respect to particle velocity \bar{v} ,
 F is the Fresnel reflection coefficient for
backward lobe,
 $d\omega$ is unit frequency,
 $d\Omega$ is unit solid angle,

and the number of photons in the frequency interval $(\omega_1 - \omega_2)$ is

$$N = \frac{2\alpha}{\pi} |\ln(2\gamma) - 1/2| \ln \omega_2/\omega_1 \quad (2)$$

where $\alpha = 1/137$, the fine structure constant (cgs).

The latter expression indicates that the mechanism is not bright in an integral sense (~ 1 photon per 100 e^-) but the radiation is relatively concentrated in a cone of opening angle $\pm 1/\gamma$. A schematic of this is shown in Fig. 5, which also shows that the lobe structure valley depends on the e^- beam divergence, the lobe peak intensity goes as γ^2 , and the spectral intensity goes as $1/\lambda^2$. The radiation is radially polarized in the observation plane.

The assessment of modeling the divergence effects has been described by Rule,¹¹ where the measured intensity of the parallel ($I_{||}$) and perpendicular (I_{\perp}) components of the angular distribution pattern is

$$I_{\perp, ||} = \int d\alpha P(\alpha) I_{\perp, ||}(\theta - \alpha) \quad (3)$$

with an assumed Gaussian distribution for the angles such that

$$P(\alpha) = \frac{1}{2\pi\sigma^2} e^{-\frac{(\alpha - \alpha_0)^2}{2\sigma^2}} \quad , \quad \sigma \text{ is the rms divergence.} \quad (4)$$

Also, the polarization (χ) is given by

$$\chi = \frac{I_{||} - I_{\perp}}{I_{||} + I_{\perp}} \quad (5)$$

Sensitivity to divergence effects in certain regimes can be enhanced by using a two-foil OTR interferometer initially

suggested by Wartski.⁹ This is schematically indicated in Fig. 6 where the forward lobe from the first foil can interfere with the backward lobes of the second foil for relativistic charged particles passing through the assembly. The previous single lobe angular distribution pattern then becomes modulated in such a way that the fringe location or relative amplitude depends on beam energy (or γ , the Lorentz factor), and the visibility of the fringe depends again on divergence and energy. Proper choice of the foil spacing depends on γ , λ , and the divergence regime of interest. At large divergences the interference fringes are obscured and the pattern reverts to the single foil angular distribution envelope. At lower γ 's we have found that we must also consider the effects of the clear foil amplitudes from the first interface of the two-foil system. This effect was described by Rule, et al.,¹⁵ and illustrated in Fig. 7, where the fringe visibility is seen to be dramatically changed for certain regimes of parameters. Finally, we comment in passing that the mechanism is generated quite promptly compared to 10 ps so it has a good chance of being used also for temporal measurements.

Cherenkov radiation¹⁶ has been used more routinely for imaging relativistic charged-particles, which transit a medium of index of refraction n with velocity $\beta = v/c \rightarrow 1$ and will not be reported in detail here. Its opening angle $\theta = \cos^{-1} 1/\beta n$ (where $\beta n > 1$) is very large compared to OTR's $1/\gamma$ for highly relativistic beams. Other aspects are that its angular distribution and intensity saturate rapidly as $\beta \rightarrow 1$, its spectral intensity goes as $1/\lambda^3$, and it is a prompt mechanism compared to 10 ps. Its emitted photon number in the visible is more like 10 per electron per mm of material. Therefore, it should be noted that to avoid thickness effects in the converter when imaging submillimeter beams, one would be led to use thinner screens whose photon yield starts approaching that of OTR in a specific solid angle.

Synchrotron radiation is emitted by charged particles under the effects of accelerations/forces in bends (usually ascribed to circular accelerators) and can be used to determine properties of those charged-particle beams as described elsewhere in this Workshop.¹⁷

Spontaneous emission radiation (as it is called in the FEL community) is actually enhanced synchrotron radiation via an undulator or wiggler. A static, alternating, and periodic magnetic field structure produces "instantaneous" circular orbits that can provide reinforcements in the angular distribution patterns at specific angles and wavelengths. The standard resonance relationship in such a situation is given by the following relationship,

$$\lambda_{obs} = \frac{\lambda_w}{2\gamma^2} [1 + A_w^2 + (\gamma\theta)^2] \quad (6)$$

where

λ_w is the period of the magnetic structure,
 γ is the Lorentz factor,
 A_w is the wiggler field parameter, and
 θ is the angle with respect to the particle velocity.

Many synchrotron rings use these undulators to provide enhanced sources of x-rays, but we have found at $\gamma \sim 220$ the visible radiation from the Tapered Hybrid Undulator (THUNDER) at the Seattle, WA, FEL facility¹⁸ can be used to great advantage to characterize the electron beam. Because the SER spectral breadth is $\sim 1/N$ for an ideal electron beam and wiggler, and $N = 220$ in that system, we have actually deduced e-beam energy centroid, energy slew, and energy spread from SER spectra. This is in addition to monitoring the beam position and profile (in a convolved sense), the brightness, and the micropulse duration.³ Examples will be given in Section III.

Advanced Electro-Optic Techniques and Adaptations

Although some of these techniques may exist in other laboratory research experiments, the adaptation of the following techniques to RF-linac-driven FELS, and in particular the characterization of e-beam properties is in the development/demonstration stage.

The Los Alamos streak/spectrometer system was installed on the Boeing visible FEL experiment in January 1988. Although initially only designed to measure the e-beam micropulse duration via SER, it was soon extended to cover other time-resolved aspects of the SER properties. A schematic view of the oscillator cavity is given in Fig. 8 showing the resonator leg, the end mirrors, the wiggler, the e-beam spectrograph, and the pop-in mirror (which allows the interception of the SER from the single passage of the electrons through the wiggler). This radiation is relayed optically to a diagnostics table in the control room over 30 m away. Figure 9 shows a layout of the streak/spectrometer, which is based on a Hamamatsu C1587 synchroscan streak camera mainframe, a 1/4-m Jarrell-Ash monochromator, a SIT readout camera, and a microcomputer for data acquisition, analysis and display. The mirrors M1S and M2S direct the radiation through the monochromator (which is used as a spectrometer), and the wavelength dispersed information is directed onto the entrance slit of the streak camera. This information can be time-resolved on the submicropulse or submacropulse domains via the fast and slow sweep plugins, respectively. With these mirrors removed, direct time-resolved spatial information can be obtained.

Additionally, the synchroscan plugin unit, which can be phase-locked to a reference 108.33 MHz frequency, provides the capability of synchronously summing the micropulses with about 4-ps (FWHM) jitter and 5-ps (FWHM) resolution. The jitter

specification is three to four times better than that of the single fast sweep unit and allows critical phase information to be monitored. This is further extended by a dual sweep attachment, which adds a slow, horizontal deflection ramp to the streak tube during synchroscan operation as shown in Fig. 10.¹⁹ Then one can measure micropulse length and phase during the macropulse. The data to be presented are the first (to our knowledge) on a FEL anywhere, and the first on an accelerator in the USA. The issue of phase stability (jitter and/or slew) is particularly critical for RF-linac e-beam parameter stability and even more so if used to drive a FEL.

III. EXPERIMENTAL RESULTS AND DISCUSSION

Having provided some background of experimental procedures in the previous section, it is hoped the series of experimental results that will now be presented will graphically illustrate our techniques.

OTR Demonstrations

For electron beams of $\gamma = 30-35$, we routinely imaged the beam spots and determined position and transverse profiles. Examples of this are shown in Fig. 11, where a single micropulse from different shots on two different screens are shown. The x- and y-profiles are given below.

Comparison of such profile data to a Gaussian distribution in Fig. 12 led us to use such a description as a working assumption. We then tracked emittance versus transported charge from our HIBAF photoinjector as shown in Fig. 13. We see strong evidence for HIBAF's meeting design goals of $\epsilon_N < 50 \text{ } \mu\text{m mrad}$ at 5 nC. These data were subsequently supplemented by macropulse measurements under a variety of conditions.⁶ Figure 14 illustrates the need for coherent amplitude terms in the divergence measurements of values less than one mrad. Table II supports these with a summary of divergence and emittance measurements for three experimental cases of solenoidal field strengths at the PEI. The trend in emittance and divergence as compared to the integrated numerical experiment (INEX) calculations is very encouraging.

At higher beam energies ($\gamma = 215$) in experiments at Boeing, we had several successes. For the particular fused silica-polished metal mirror geometry, the predicted competition of sources that could blur the total beam spot was observed. This effect is shown in Fig. 15 schematically and Fig. 16 experimentally. A very successful interferometer experiment was also performed. As shown in Fig. 17, the interferogram for a calculated divergence of $\sigma_{rms} \sim 0.3 \text{ mrad}$ and $E = 107 \text{ MeV}$ is a good match to the data. Additionally, an energy sensitivity is shown in the amplitudes of the two inner peaks as illustrated by comparing calculated curves at 107 and 109 MeV to the same data in

Fig. 18. The energy and divergence effects are somewhat separated in this manner, and thus gives hope to having the 1% energy accuracy for the technique. It is also noted that the centering of the OTR pattern relative to the reference alignment laser in angle and transverse position provides a pointing capability from a single axial location. This feature might be used to help match the e-beam into a FEL wiggler. Another graphic example on spatial resolution is shown in Fig. 19. In this case, nine of the eleven alumina screens in the Boeing/STI 5-m wiggler were replaced with diamond-polished aluminum screens with a thin metal mask in front of them. In this situation, the visible SER had to be blocked from the path to the cameras to avoid overwhelming the OTR visible radiation. The limiting resolution (~ 0.5 mm) is indicated by the observed radius from the alumina screen (W11) being much larger than the OTR-measured spots. Improved pointing and matching in the wiggler led to an improved small signal gain for the FEL.

Before leaving this category, I note that at a SLAC workshop²⁰ I reported the possibility of 50 μ rad type divergence measurements on those electron-beams at very high γ . Also, some profiling measurements of 450 GeV protons at CERN have been done with OTR techniques and the reader is referred to those articles.^{21,22} In that work, thinner OTR foils (~ 3.5 μ m) were possible than those used for secondary emission foil techniques (~ 100 μ m thick) so beam scattering was reduced.

The OTR technique compares favorably with standard e-beam emittance diagnostics that rely on measurement sequences (quadrupole field variation) at one screen position or two. In closing this subsection, a list of some of the advantages and disadvantages is presented.

Several Advantages:

1. Measurements are possible on a single macropulse,
2. Data structure and theory allow on-line evaluation of emittance,
3. A single position in the beamline can be used for e-beam profile, divergence, and angle (pointing) measurements,
4. Thinner screens (foils) reduce beam scattering and x-ray production,
5. OTR provides a simultaneous e-beam energy diagnostic ($\sim 1\%$ accuracy), and
6. Thinner screens and single shot mode should reduce vacuum degradation near the photocathode of injectors.

Disadvantages:

1. Source brightness,
2. Required careful optical alignments and parts, and
3. Convolution of divergence and energy effects.

Spontaneous Emission Radiation Results

These experimental results include the nonintercepting measurements of e-beam position, profile, charge, pulse length, and energy. They are intertwined with the streak/spectrometer, synchroscan, and dual sweep measurements.³ As an example, Fig. 20 shows the integrated effects of beam centering change during the macropulse. In Fig. 21 beam bunching is measured/diagnosed before (upper) and after (lower) adjustment of the subharmonic buncher phases in the injector. The decrease in observed pulse length from 28 ps to 12 ps (FWHM) is important to FEL operations. The e-beam energy centroid, width, and slew can be deduced from the SER time-resolved spectra given in Figs. 22 and 23. The HeNe laser reference illustrates the instrumental limiting resolution of ~2.2 nm.

Streak Spectrometer Applications

A few additional demonstrations of streak/spectrometer results are shown by Fig. 24 and Fig. 25. The first one shows the first direct measurement of a wavelength shift within a FEL micropulse (~3 nm in 8 ps).² The second shows an example of the suppression of a long-wavelength sideband by a simple 8-10 μ m cavity length detuning as monitored during the macropulse (~100 μ s).²³ Such time-resolved information was critical to understanding the FEL evolution.

Synchroscan and Dual-Sweep Streak Techniques

It has been determined that low-jitter synchroscan streak measurements can be used to diagnose phase and pulse length during the macropulse (with dual-sweep). A number of examples are briefly cited.

Our ability to evaluate some key dynamic issues in the HIBAF photoelectric injector was greatly enhanced by using the synchroscan feature.⁴ Figure 26 shows a schematic of the PEI accelerator with photocathode inserted into the wall of the first cell. Upon irradiation by the pulsed drive laser operating at 527 nm and 10 to 15 ps pulse length, the electrons are released and immediately accelerated by a 26 MV/m gradient to relativistic velocities. At a downstream screen, the electron beam micropulse information is converted via Cherenkov radiation and detected in the streak camera. Using path-length matching, a fraction of the drive laser light is also relayed to the same streak camera and streak sweep. Figure 27 then shows the simultaneous measurement of these two pulses. By adjusting the phase of the drive laser relative to the RF cycle, we mapped out the effects on e-beam elongation and transit time as shown in Figs. 28 and 29. These were the first successful measurements of their kind on a PEI and contributed to the qualification of the space-charge calculations in our simulations program (basically PARMELA).

Another aspect involved the ability to track shot-to-shot phase stability relative to the 108.3 MHz.⁵ Fig. 30 shows a series of 16 macropulse averaged temporal profiles indicating quite noticeable jitter is occurring (~ 1.6 ps/ch). In response to suggestions that this was streak camera jitter, we acquired a coordinated set of temporal positions versus e-beam energy centroid detected in the electron spectrometer. As shown in Fig. 31, a strong correlation was observed with a sensitivity of about 0.1% energy shift per picosecond of phase. The extreme cases of phase shifts greater than 5 ps were difficult to track due to the span of energy covered and the loss of image brightness. Significant improvement in the drive laser phase stability was demonstrated with the addition of a commercially available phase stabilizer to the ND:YLF oscillator system. Figure 32 shows the reduction of the rms jitter from 10.9 ps to 1.7 ps (about the camera limit). These data further exonerated the streak camera jitter specification of 4 ps (FWHM).

Another unexpected use of the synchronous summing of micropulses involved our ability to provide temporal information in the 10-ps domain about field-emission electrons. The picocoulomb magnitude charge generated at the peaks of the RF cycle were synchronously summed into usable images as shown in Fig. 33. Transport conditions could result in only some of the electrons being sampled, and these had a surprising 20-ps FWHM structure.

Finally, referring back to the SER discussion, the final synchronous sum of 12 ps (FWHM) still includes intramacropulse jitter and/or slew. The nature of these were assessed by turning on the dual sweep streak feature.⁵ As shown in Fig. 34, most of the macropulse shows the effect of the buncher phase adjustment. These results are tabulated in Table 3 and indicate that in the tuned case, the synchronous sum of 10 ps may include jitter and/or slew that expands the individual 8-ps width out to 10 ps. Additionally, in Fig. 35, the visible lasing macropulse has a modulation of ~ 13 - μ s period during the macropulse, while simultaneously we measured the 8-ps lasing pulse length.

IV. SUMMARY

In summary, a number of graphic demonstrations of these advanced imaging applications have been cited, albeit somewhat briefly. Of particular note in our investigations have been the use of CTR and SER conversion procedures to reveal e-beam (or charged particle beams) parameter information. The radiations from these conversion processes then have been imaged in time-resolved modes on a wide range of timescales that are generic to RF-linac driven electron beams (and FELs). We have particularly found useful the low time jitter of synchroscan streak cameras and the extension to multiple time domains with dual-sweep techniques. These techniques have been presented to the Workshop participants in hopes of stimulating their adaptation to other accelerator-based systems for charged-particle beams.

ACKNOWLEDGMENTS

The author acknowledges the assistance of N. S. P. King and M. D. Wilke of Los Alamos and S. P. Wei of Boeing for integrating the streak/spectrometer at Boeing, the collaboration with D. W. Rule and R. B. Fiorito on OTR experiments and analyses, and discussions with J. C. Goldstein of Los Alamos on spontaneous emission radiation phenomena.

REFERENCES

1. A. H. Lumpkin and D. W. Feldman, Nucl. Inst. and Meth. A259, (1987), p. 49.
2. A. H. Lumpkin, N. S. P. King, M. D. Wilke, S. P. Wei, and K. J. Davis, Nucl. Inst. and Meth. A285, (1989), p. 17.
3. Alex H. Lumpkin, Nucl. Inst. and Meth. A296, (1990), p. 134.
4. Alex H. Lumpkin, Bruce E. Carlsten, and Renee B. Feldman, "First Measurements of Electron-Beam Transit Times and Micropulse Elongation in a Photoelectric Injector," presented at the 12th International FEL Conference, Paris, France, Sept. 17-21, 1990.
5. Alex H. Lumpkin, "The Next Generation of RF-FEL Diagnostics: Synchroscan and Dual-Sweep Streak Technique," presented at the 12th International FEL Conference, Paris, France, Sept. 17-21, 1990.
6. A. H. Lumpkin, et al., "Initial Observations of High-Charge, Low-Emittance Electron Beams at HIBAF," presented at the 12th International FEL Conference, Paris, France, Sept. 17-21, 1990.
7. T. C. Marshall, Free-Electron Laser (Macmillan Publishing Co., NY), 1985, and Proceedings of the 11th International Free-Electron Laser Conference, Nucl. Inst. and Meth., A296, (1990), and references therein.
8. V. L. Ginzburg and I. M. Frank, Sov. Phys. JETP 16, (1946), 15.
9. L. Wartski, et al., J. Appl. Phys. 46 (1975), 3644.
10. R. B. Fiorito, et al., Proc. 6th Int. Conf. on High-Power Beams, Kobe, Japan (1986).
11. D. W. Rule, Nucl. Inst. and Meth., B24/25 (1987), 901.
12. A. H. Lumpkin, et al., Nucl. Inst. and Meth. A285, (1989), 343.
13. A. H. Lumpkin, et al., Nucl. Inst. and Meth. A296, (1990), 150.
14. D. W. Rule and R. B. Fiorito, "Imaging Micron-Sized Beams with Optical Transition Radiation," Poster Paper this Workshop.
15. D. W. Rule, R. B. Fiorito, A. H. Lumpkin, R. B. Feldman, and B. E. Carlsten, Nucl. Inst. and Meth. in Physics Research, A296, (1990), 739.

16. J. V. Jelley, Cherenkov Radiation and Its Applications, Pergamon Press Ltd., London (1958).
17. R. J. Nawrocky and J. Rogers, "Beam Profile Measurements Using Synchrotron Light," These Proceedings.
18. K. E. Robinson, et al., Nucl. Inst. and Meth. A259, (1987) 62, and IEEE J. Quantum Electronics, QE23, (1987), 1497.
19. Y. Tsuchiya, et al., "Two-Dimensional Sweeps Expanding Capability and Application of Streak Cameras," SPIE, Vol. 693, (1986), 125.
20. Alex H. Lumpkin, "Imaging Techniques for Charged-Particle Beam Diagnostics," International Workshop on Next Generation of Linear Colliders, Stanford Linear Accelerator Center, Palo Alto, CA, Dec. 6, 1988.
21. J. Bosser, J. Dieperink, G. Ferioli, J. Mann, L. Wartski, IEEE Trans. on Nucl. Science, Vol. NS-32, No. 5, October 1985, p. 1905.
22. J. Bosser, J. Mann, G. Ferioli, and L. Wartski, CERN/SPS/84-17 (AB).
23. A. H. Lumpkin, et al., Nucl. Inst. and Meth. in Physics Research A296, (1990), 169.

FIGURES

Fig. 1. Schematic of a RF-linac driven FEL.

Fig. 2. Schematic of the e-beam pulse structure for an FEL with a 7-m long cavity.

Fig. 3. Schematic of HIBAF beamline and diagnostic stations (OTR; CH).

Fig. 4. Schematic of OTR and CH patterns: (a) normal incidence, (b) oblique incidence ($\phi = 45^\circ$); Cherenkov radiation, $\theta \sim 46^\circ$.

Fig. 5. A schematic representation of the single-foil OTR angular-distribution pattern dependence on e-beam parameters, where γ is the Lorentz factor.

Fig. 6. Schematic of two-foil OTR interferometer.

Fig. 7. A comparison of calculated interferograms with and without the clear foil's first interface coherent amplitudes.

Fig. 8. A schematic view of the Boeing burst-mode oscillator cavity (not to scale). CM: current monitor, SC: screen.

Fig. 9. Schematic of the Los Alamos streak/spectrometer system located on the burst-mode control room diagnostics table.

Fig. 10. Schematic of the synchroscan and dual sweep features of the streak camera.

Fig. 11. A composite set of beamspot images and profiles for stations 2 and 3 at HIBAF.

Fig. 12. Gaussian-shaped profile compared to experimental spatial profile (box average of single micropulse image).

Fig. 13. Emittance versus charge for a single micropulse with comparison to INEX and FELPPC codes.

Fig. 14. Comparison of theory and experiment with calculated patterns using rms divergence of 0.9 and 0.7 mrad.

Fig. 15. Schematic of the reference fused-silica and metal mirror assembly sources involved in the beamspot images.

Fig. 16. Experimental example of the multiple source problem on a beamspot.

Fig. 17. Initial interferometer image (top) and match to its horizontal profile (bottom) with an electron beam energy of 107 MeV and a divergence of ~ 0.3 mrad.

Fig. 18. Calculated interference patterns for 107 and 109 MeV compared to experiment show e-beam energy effect.

Fig. 19. Plot of spot sizes obtained before and within the 5-m wiggler: (a) vertical plane, and (b) horizontal plane. The resolution blur caused by the alumina screen W11 is noticeable compared to the OTR-screen spots.

Fig. 20. A $6\text{-}\mu\text{s}$ sampling of the e-beam spatial position versus time using SER.

Fig. 21. Electron beam micropulse bunching measurement using visible SER in Boeing Facility before (upper) and after (lower) tuning the injector.

Fig. 22. A 30-macropulse average of the time-resolved SER spectrum (upper) and HeNe reference (lower). The e-beam energy and spread can be determined.

Fig. 23. Selected spectra from macropulse time intervals $30\text{-}\mu\text{s}$ apart in Fig. 22. A small centroid shift is attributed to e-beam energy slew.

Fig. 24. Streak/spectrometer data for a single lasing micropulse (<10 ps) showing a wavelength difference in 8 ps.

Fig. 25. Time-resolved lasing spectra for a $63\text{-}\mu\text{s}$ span for cavity detuning of 0 and $8\text{ }\mu\text{m}$.

Fig. 26. Schematic of photoelectric injector accelerator.

Fig. 27. "Simultaneous" synchroscan streak images of 17-MeV e-beam (Cherenkov converter) and drive laser micropulses.

Fig. 28. Electron-beam micropulse length variation with drive laser phase changes.

Fig. 29. Electron beam transit time effects versus drive laser phase in the photoinjector.

Fig. 30. Synchroscan streak profiles tracking drive laser phase jitter.

Fig. 31. Correlation of phase jitter of Fig. 30 to electron beam energy jitter at spectrometer.

Fig. 32. Synchroscan streak measurement of drive laser intermacropulse jitter with and without phase stabilization.

Fig. 33. Beamspot (upper) and synchroscan streak image (lower) of field emission electrons at 17 MeV.

Fig. 34. Initial dual-sweep streak images of 109-MeV e-beam using SER with injector phased and dephased.

Fig. 35. Initial dual-sweep streak image of the visible FEL output from the ring resonator showing macropulse temporal structure (upper) and micropulse bunch length measurement (lower).

TABLE I. ELECTRON BEAM PARAMETERS AND THEIR DIAGNOSTICS (HIBAF)

Parameter	Nominal Value	Span	Technique	Resolution	Error	Timescale
Position	Reference to laser line	± 10 mm	OTR screens	~ 50 μ m	< 100 μ m	Single-micro, or streak
Transverse Profile	1 mm, FWHM	0.5-15 mm	OTR screens	~ 50 -100 μ m	5-10%	Single-micro or streak
Divergence	1-2 mrad	0.5-3.0 mrad	Two-station OTRI	Few tenths mrad 0.4 mrad limiting	15% 15%	Single-micro macro
Emittance	50 γ mm-mrad	10-150 γ	Two-station OTRI	Depends on beam transport	(30%) (30%)	Single-micro macro
Pointing	on laser line	0-5 mrad	Two-station OTRI	~ 0.2 mrad ~ 0.2 mrad	20-30%	Submacro
Charge	5 nC	0-10 nC	Wall current monitor	0.1 nC	20%	Submacro
Energy Spread Jitter Slew	15 MeV 0.5% $\pm 0.2\%$ 0.24%	5-17 MeV	Spectrometer 90 $^\circ$ bend, Cherenkov screen	$\sim 0.2\%$	(10%)	Submacro
Micropulse Duration	10-15 ps	5-35 ps	Streak camera Cherenkov rad	2 ps (fast) 6 ps (synchro)	10-15%	Submicro
Drive Laser Jitter Slew	10-15 ps	5-25 ps	Streak camera Synchroscan Synchroscan	2 ps (fast) 4 ps over seconds < 4 ps over seconds	10-15%	Submicro
Beam Spill	Relative to no beam	--	X-ray detector	Field emission		Submacro

TABLE II. SOLENOID VARIATION EFFECTS, SIMULATION AND EXPERIMENT (OTRI)*
(May 17, 1990)

Case No.	Laser Phase	Solenoids(A)		Charge (nC)	X-FWHM (mm)	Divergence (mrad)		Emittance (mm-mrad)	
		1	2			OTRI*	INEX	HIBAF**	INEX
1	20°	25	500	3.0	0.8	1.5	2.0	65	62
2	20°	50	500	3.4	0.7	1.5	(1.5)	58	50
3	20°	75	500	3.1	0.7	0.9	1.3	36	43
4	20°	55	550	3.1	--	--	1.0	--	39

*Optical Transition Radiation Interferometry (OTRI).
**Assumed Gaussian Distributions for spot size and particle directions.

TABLE III. SUMMARY OF SYNCHROSCAN AND DUAL SWEEP
STREAK MEASUREMENTS OF e-BEAM AT BOEING
(Data of 4-13-90)

Measurement Technique	Accelerator Condition	Pulse Length* Observed (ps)	Pulse Length* e-Beam (FWHM, ps)
Synchroscan	100 μ s, as found	28	27
Synchroscan	100 μ s, 108 MHz tune	17.5	16
Synchroscan	100 μ s, 433 MHz tune	12.3	10
Dual Sweep	Phased, 100- μ s span, -10 μ s sample	10.6	8
Dual Sweep	Dephased, 108 MHz -10 μ s sample	17.2	16

$$*\Delta t_{obs} = \sqrt{(\Delta t_{eB})^2 + (\Delta t_{Res})^2 + (\Delta t_{jitter})^2}$$

where:

Δt_{eB} includes intrinsic pulse length for a single
micropulse plus jitter and slew for a macropulse
 Δt_{Res} = 6 ps of synchroscan sweep
 Δt_{jitter} = 4 ps (FWHM) over seconds specification

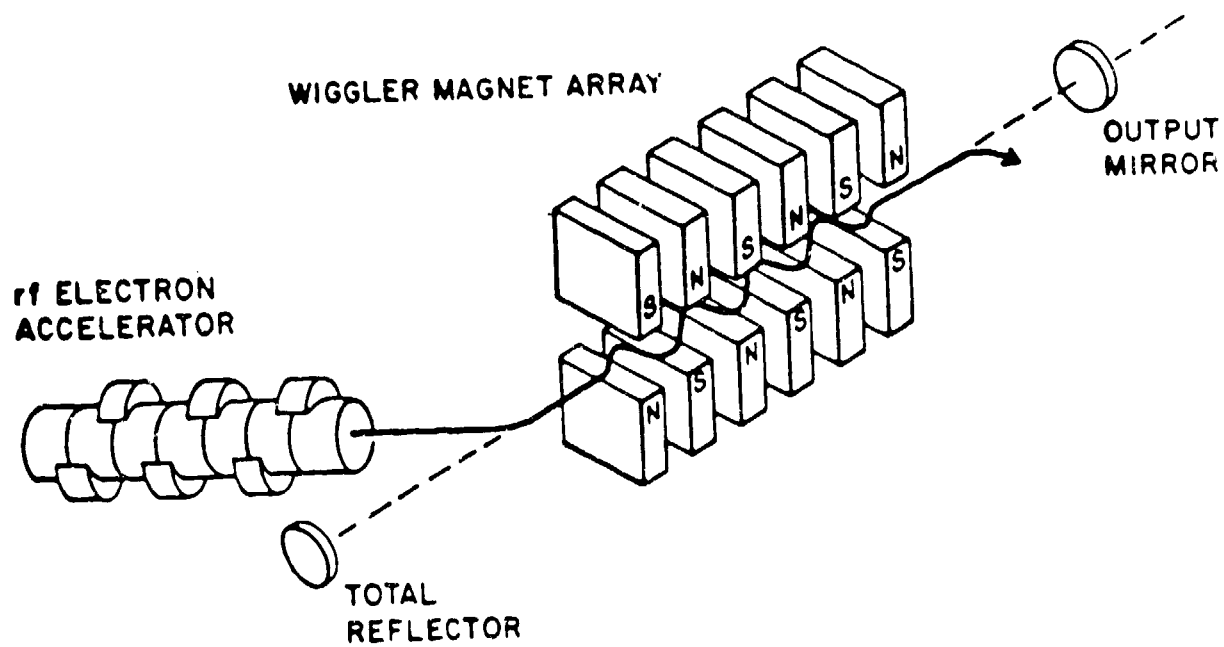


Fig. 1

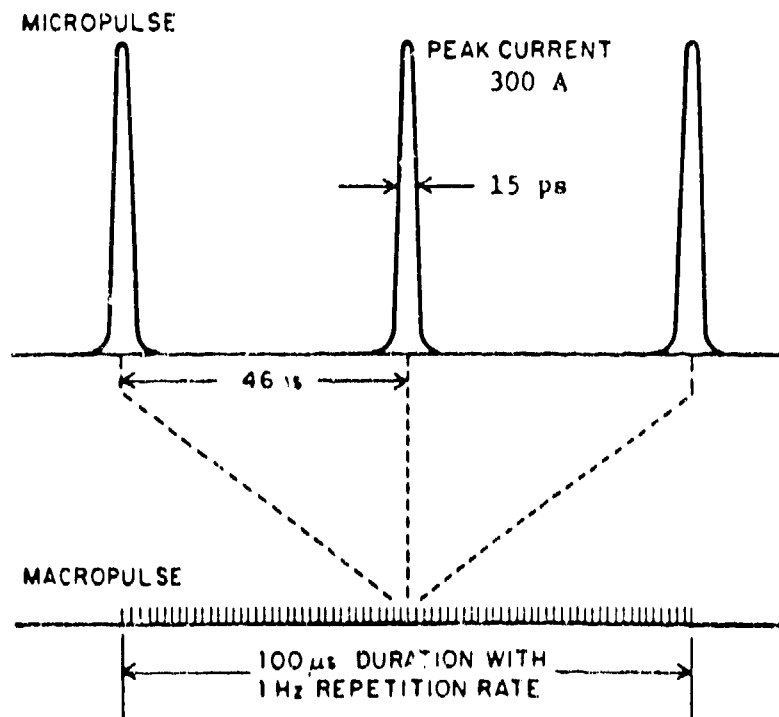


Fig. 2

NEW DIAGNOSTICS ALLOW MEASUREMENT OF CRITICAL BEAM PARAMETERS ON HIBAF

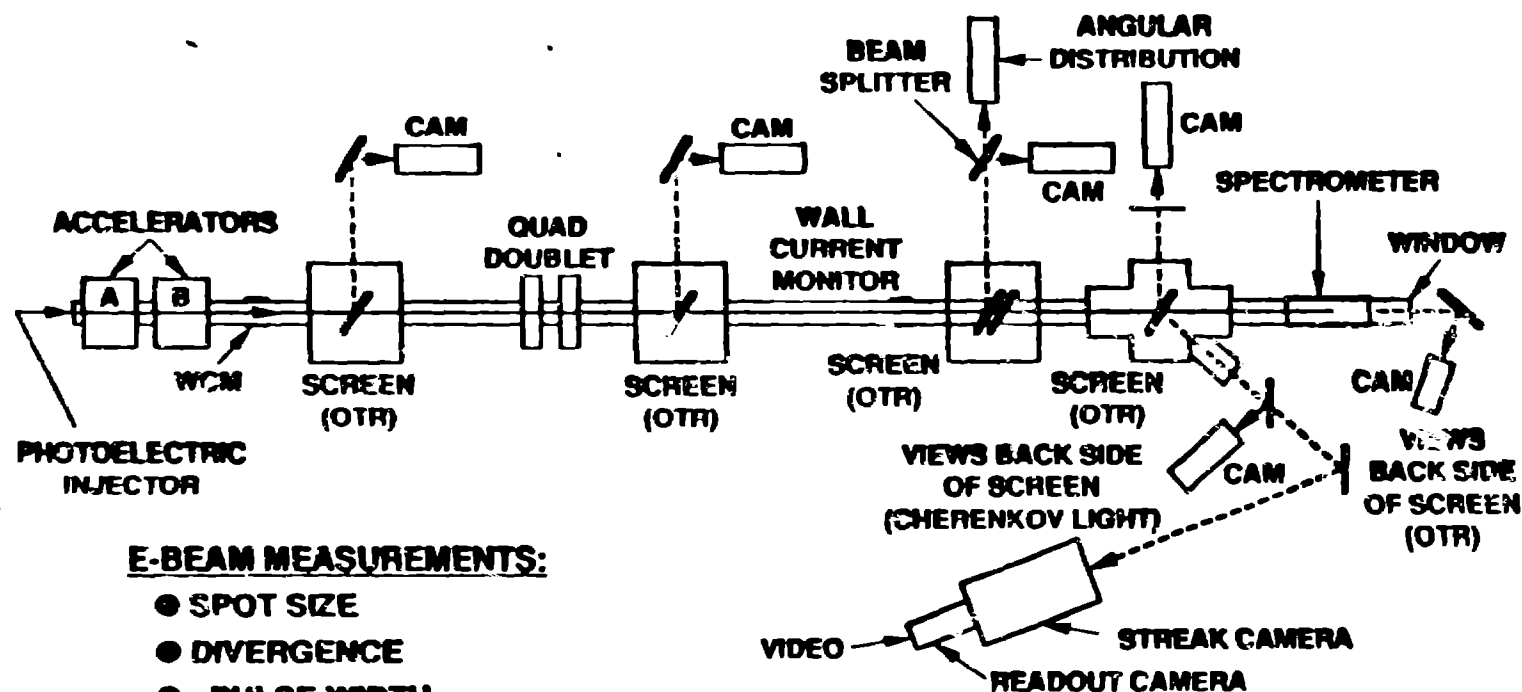
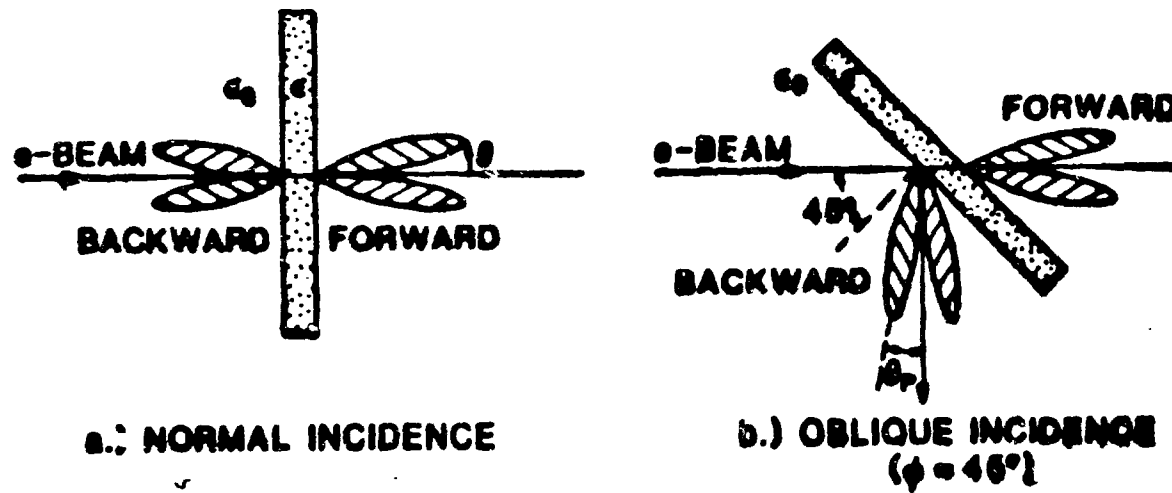


Fig. 3

OPTICAL TRANSITION RADIATION PATTERNS



CHERENKOV RADIATION PATTERN ($\theta \sim 46^\circ$)

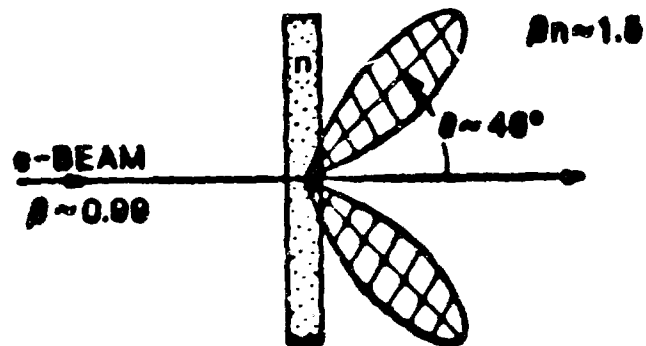


Fig. 4

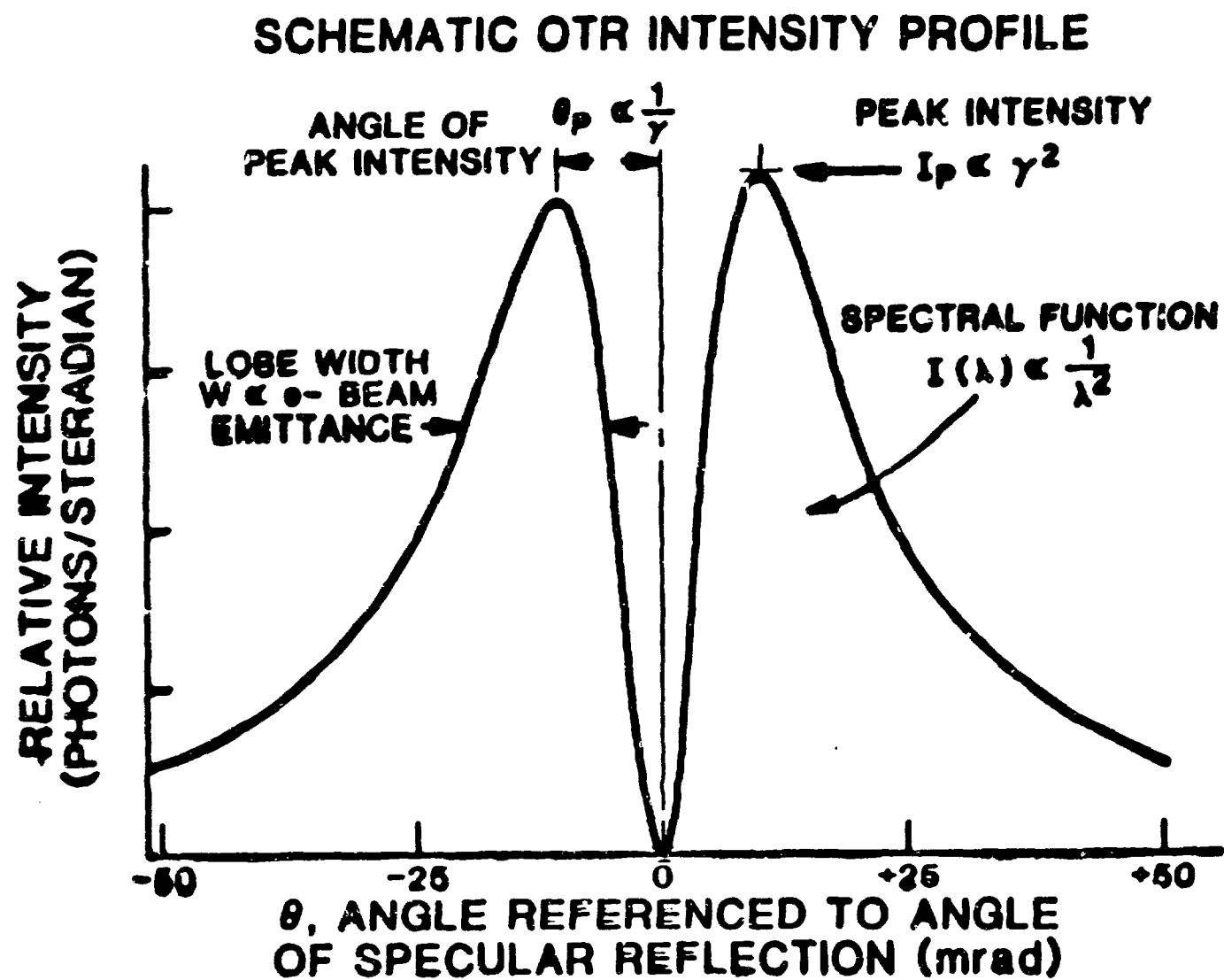


Fig. 5

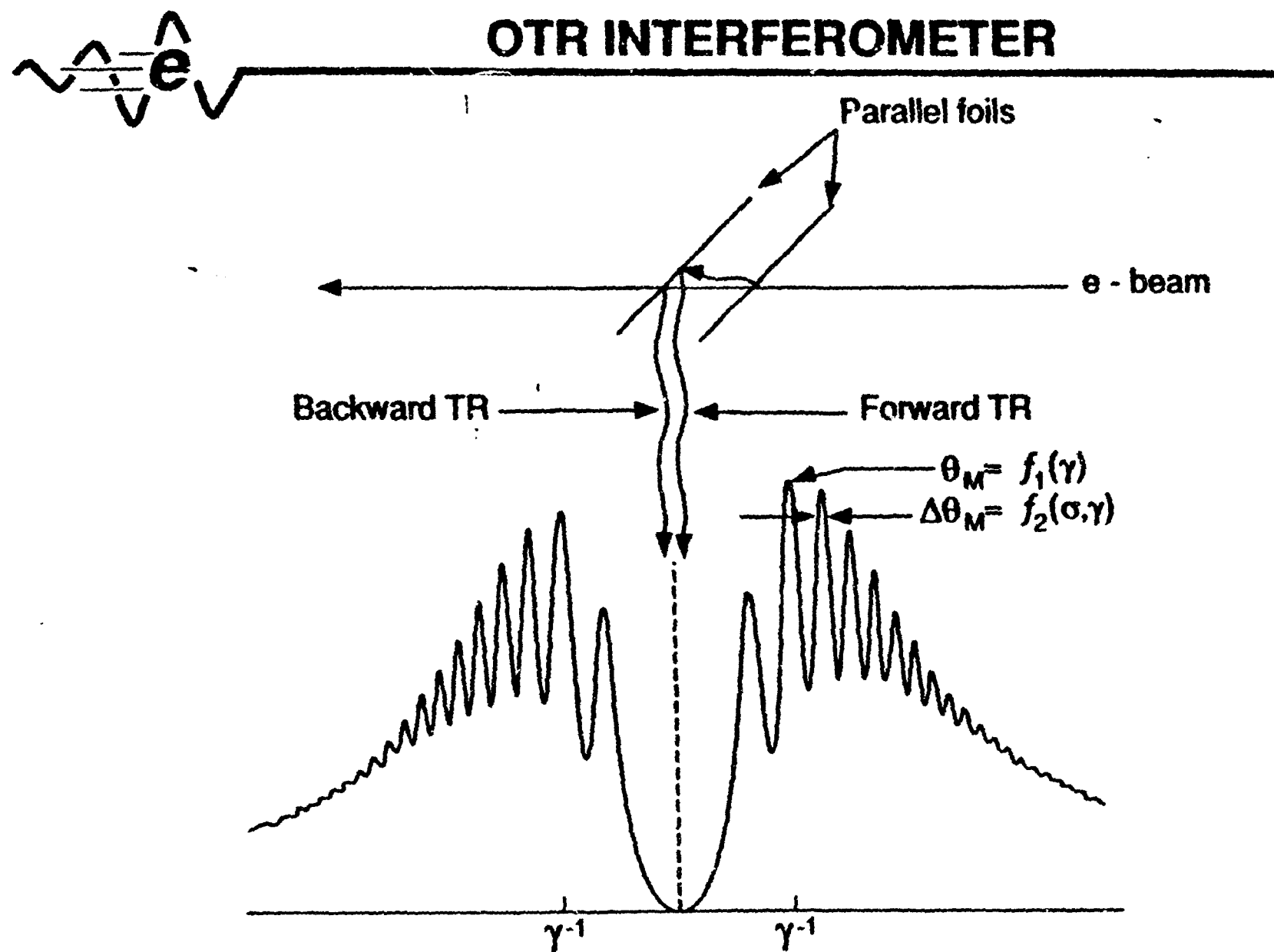
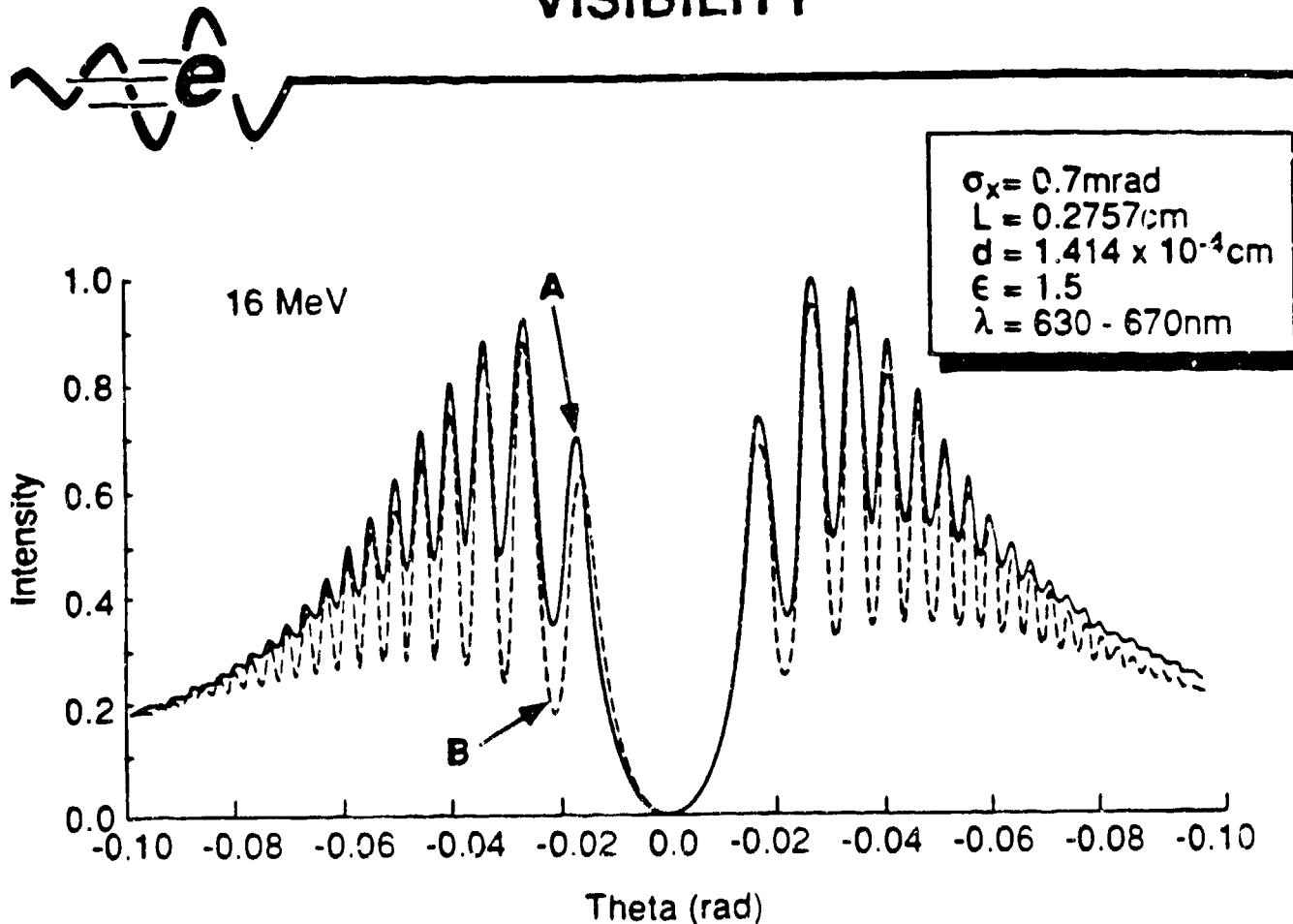


Fig. 6

CALCULATED CURVES FOR CLEAR FOIL CONTRIBUTIONS SHOW REDUCED FRINGE VISIBILITY



A: Clear foil: means coherent amplitudes from both surfaces of clear foil included.

B: Without: means incoherent intensities, both reflected and forward, from the first interface are included in an approximate way.

Fig. 7

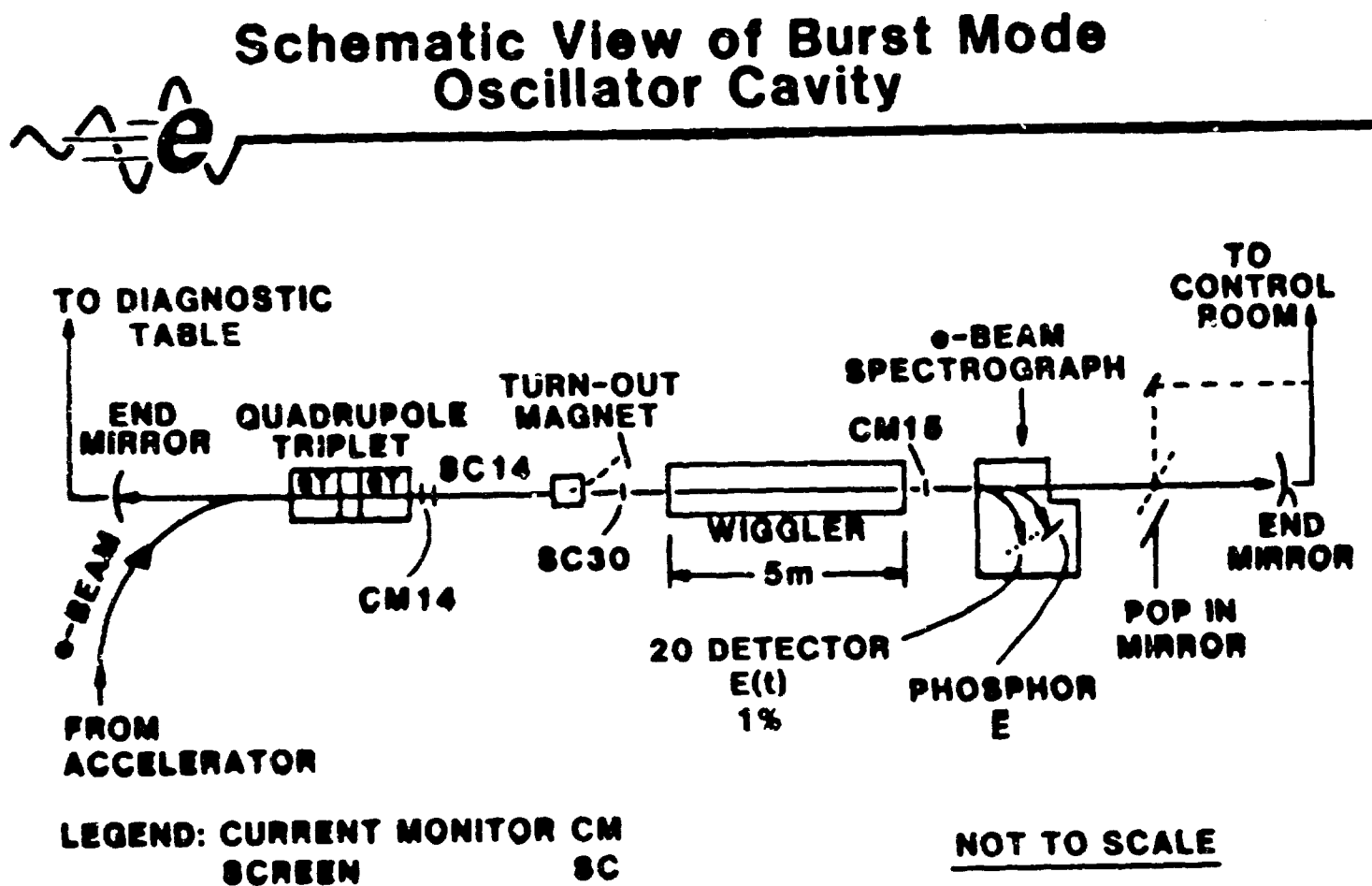


Fig. 8

Schematic Layout of Los Alamos Streak/Spectrometer System

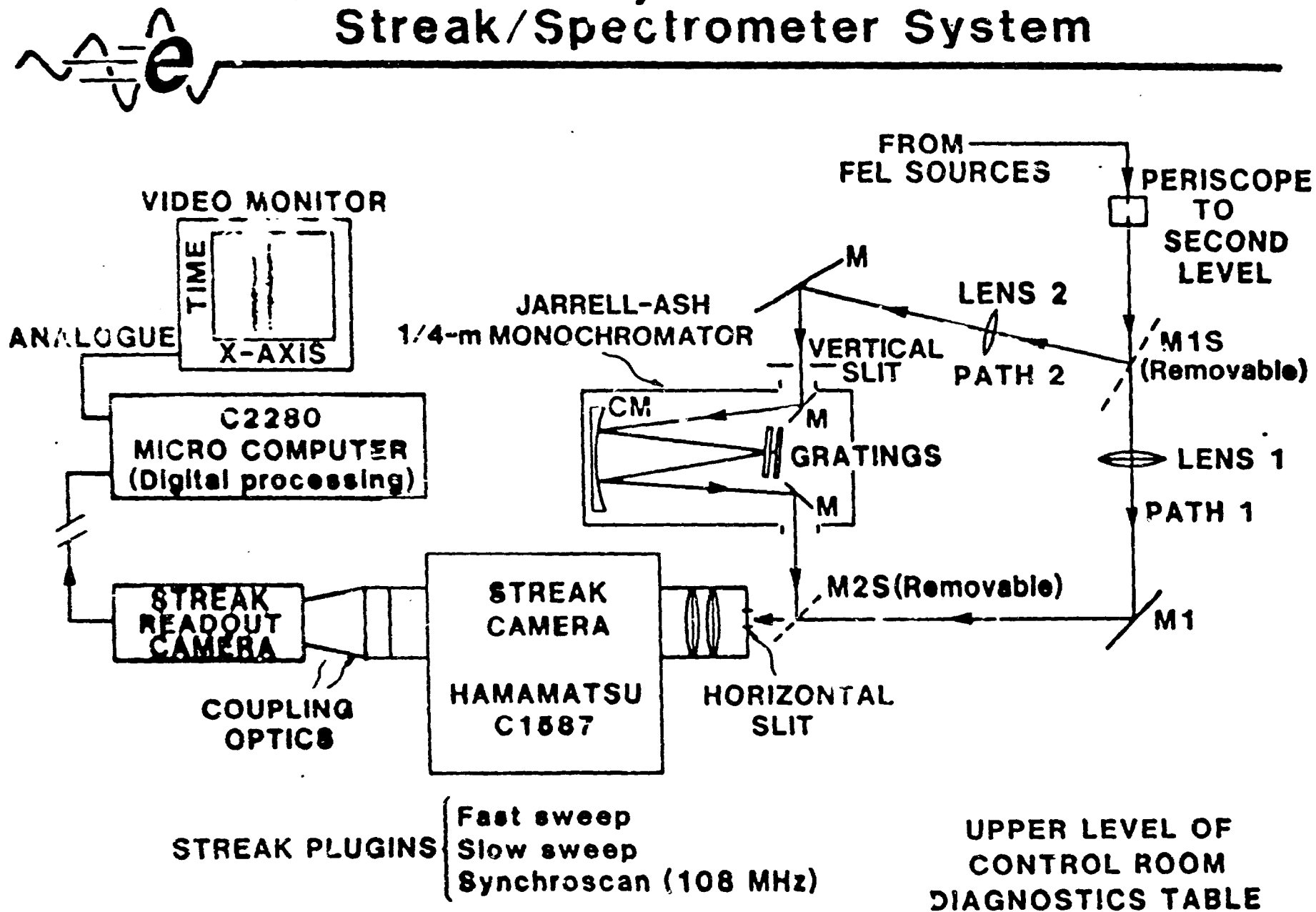


Fig. 9

SCHEMATIC OF DUAL SWEEP STREAK TECHNIQUE

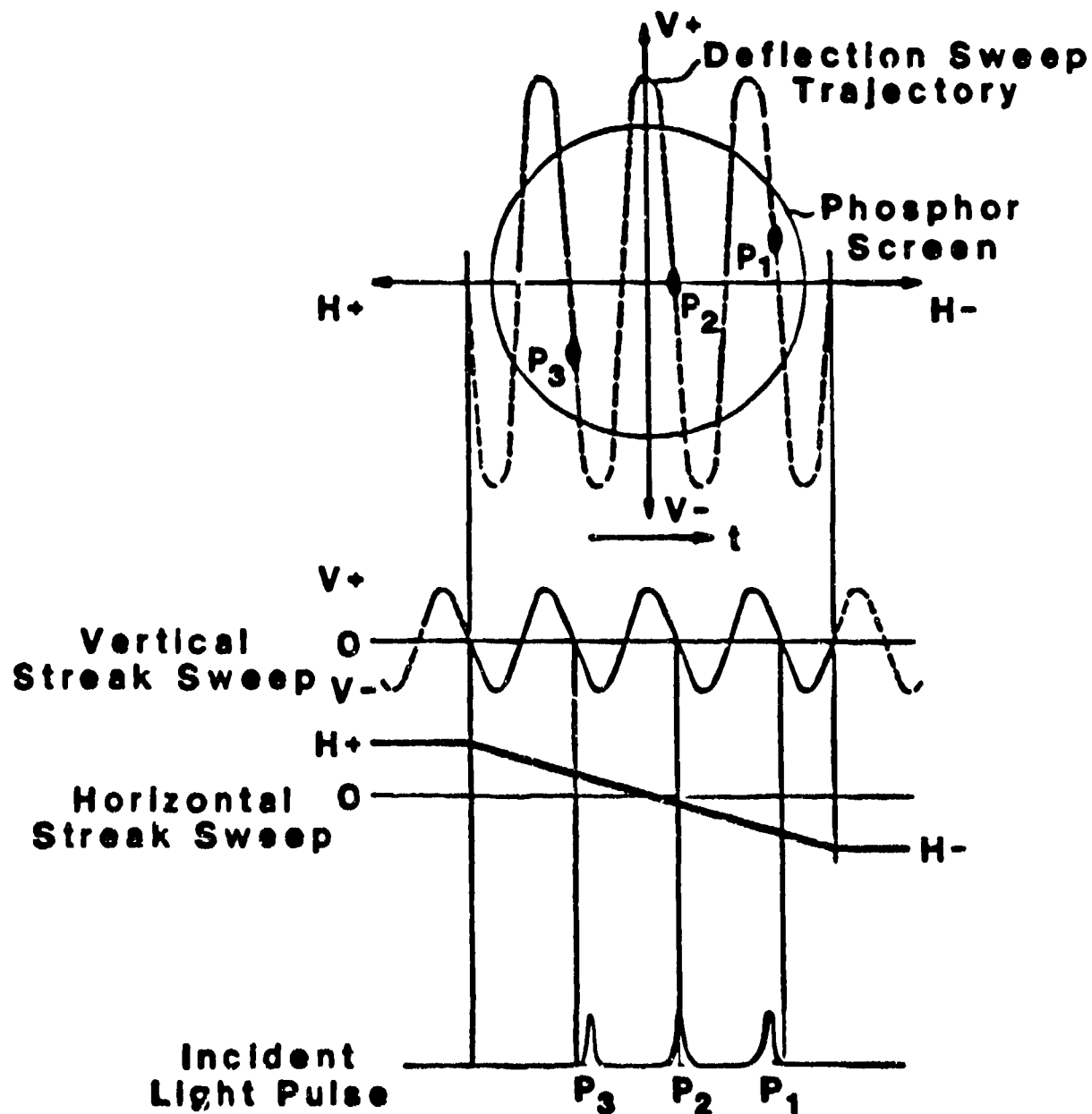


FIG. 10

**OPTICAL TRANSITION RADIATION SCREENS ARE USED TO
DETERMINE BEAM PROFILES FOR EMITTANCE MEASUREMENTS**

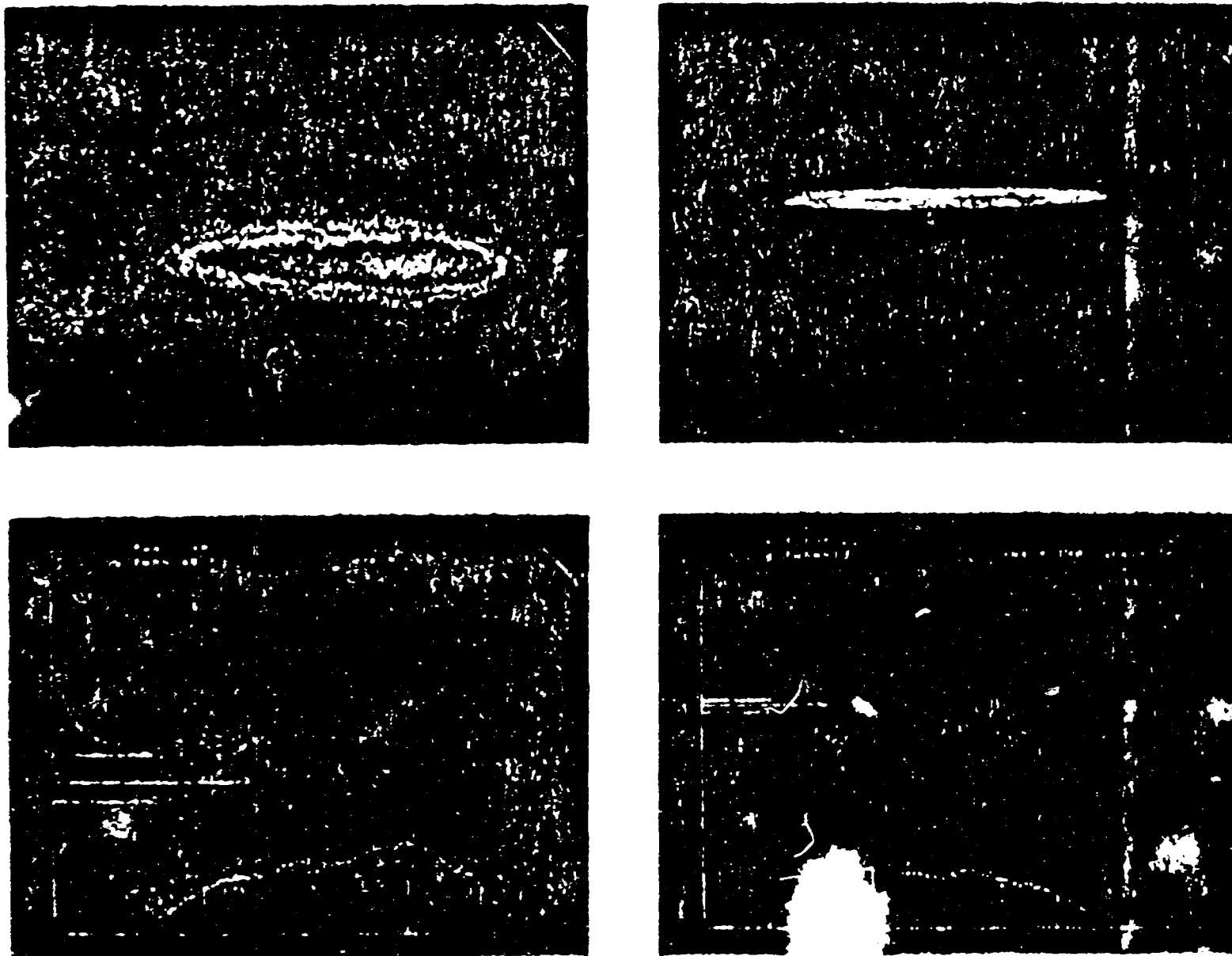


Fig. 11

BEAM PROFILE APPROXIMATED BY GAUSSIAN FUNCTION

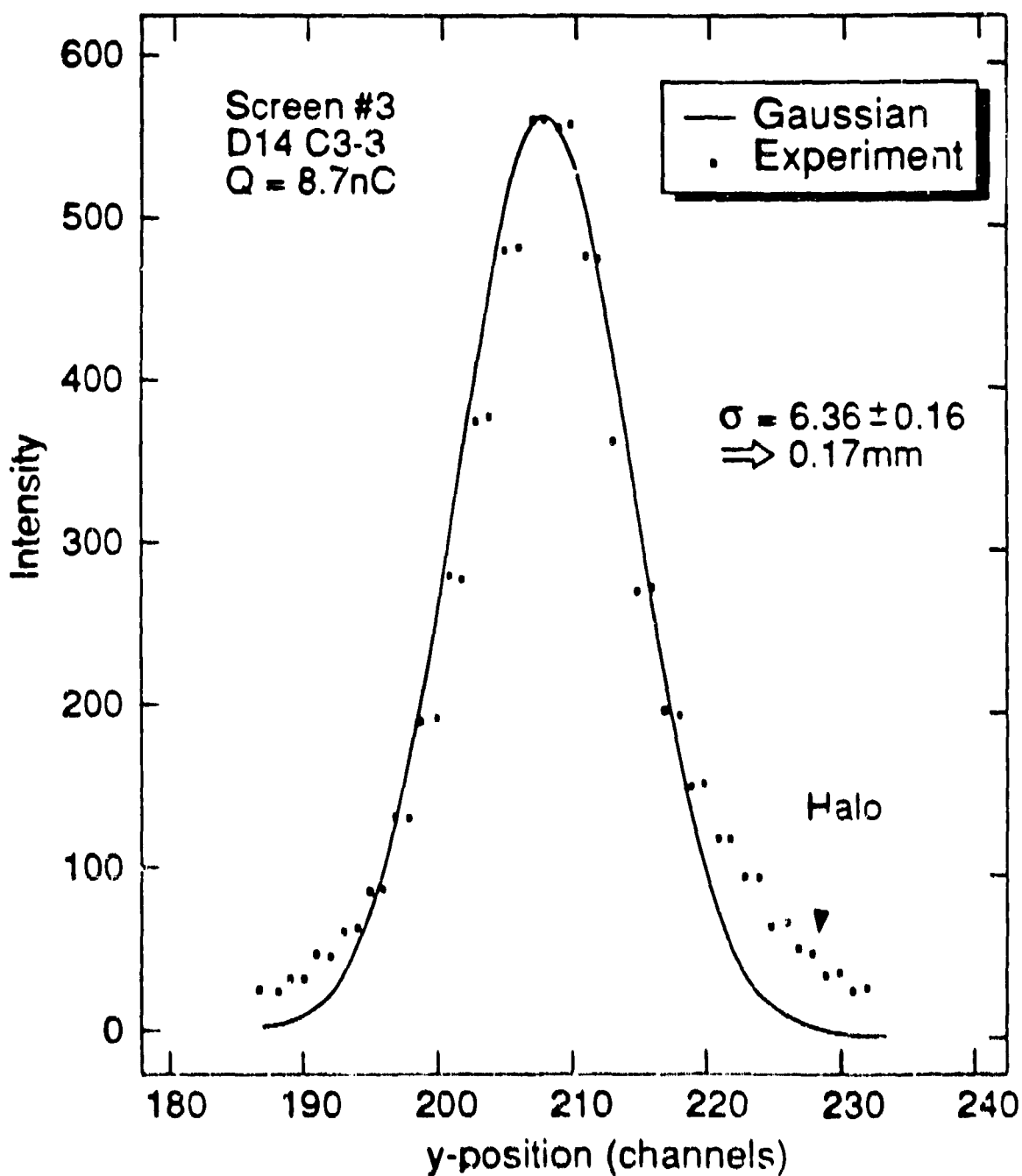
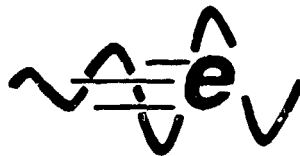


Fig. 12

DEMONSTRATED LOW-EMITTANCE, HIGH-CHARGE E-BEAMS CONSISTENT WITH INEX PREDICTIONS AND LSS REQUIREMENTS

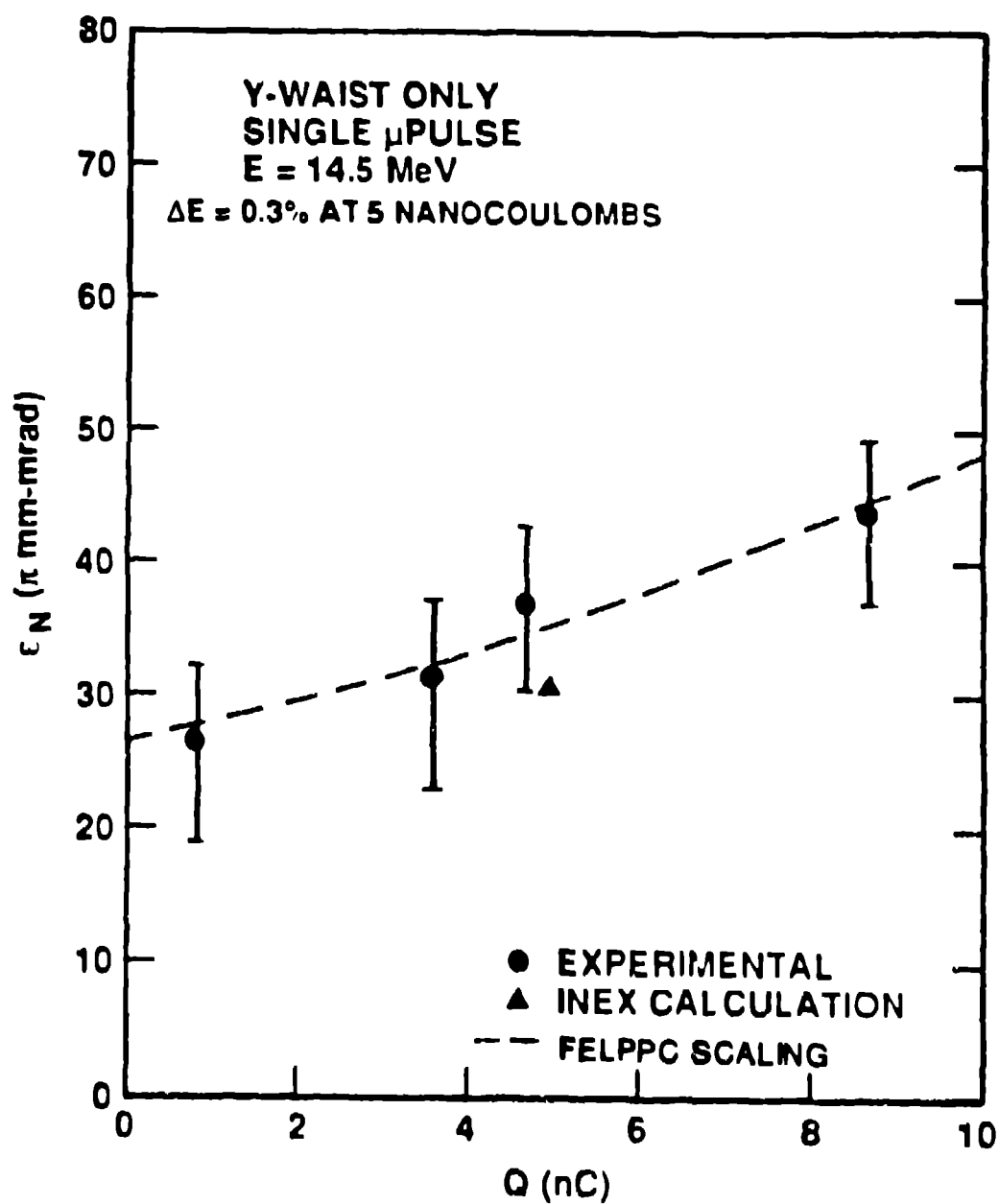


Fig. 11

COHERENT AMPLITUDES USED TO MATCH INTERFEROGRAM (HIBAF 4-4-90)

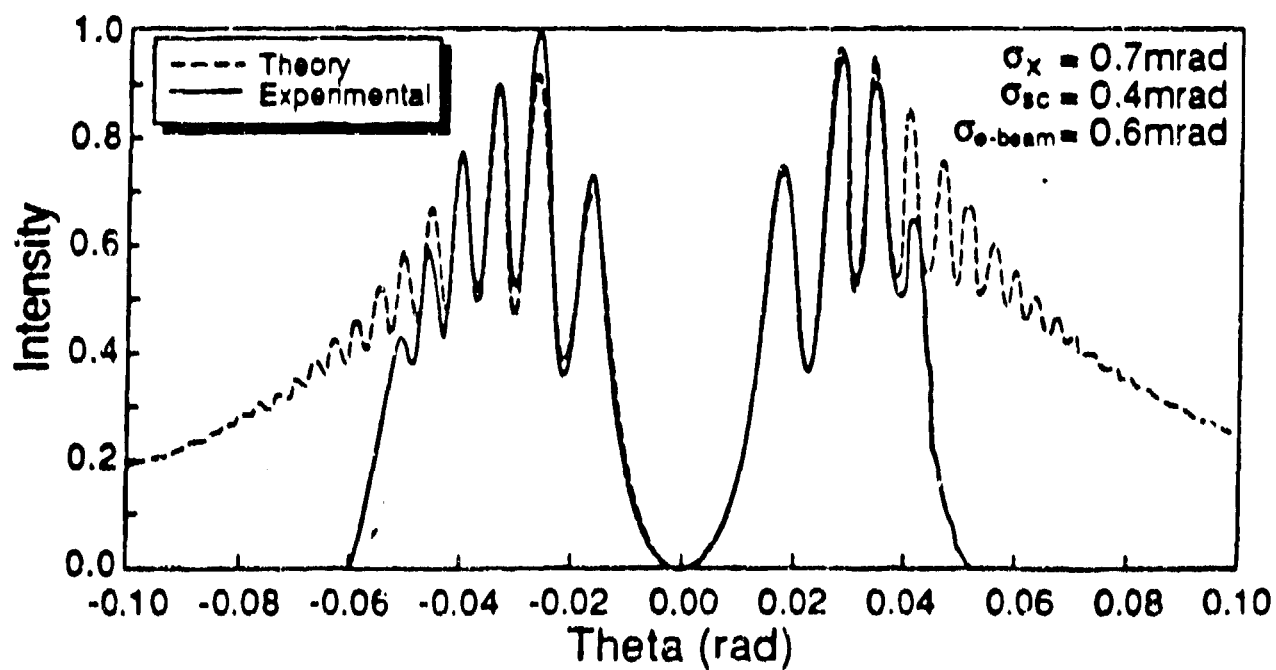
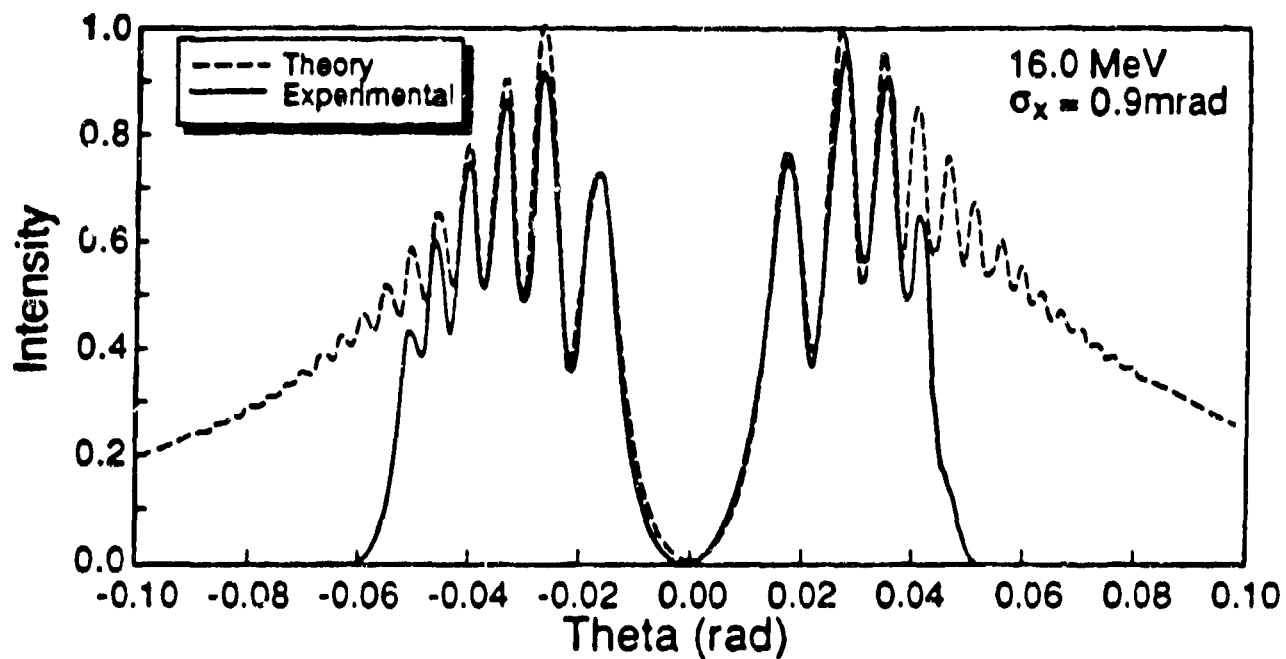
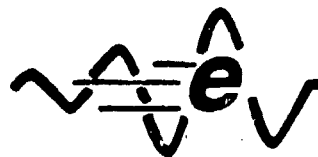


FIG. 14

Fused Silica Plus Metal Mirror Assembly Can Lead to Broadened Beamspot (scattering and alignment)

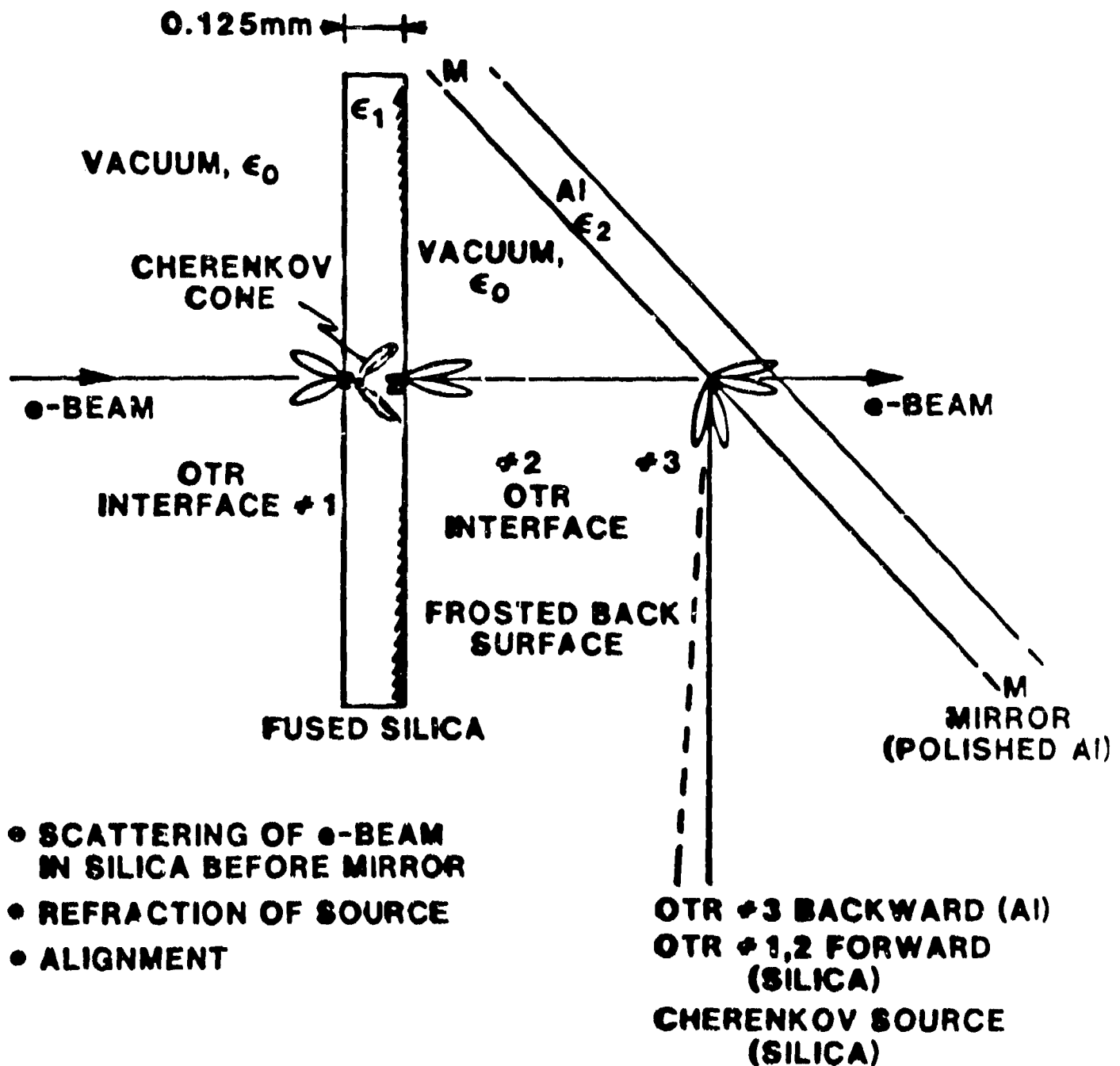
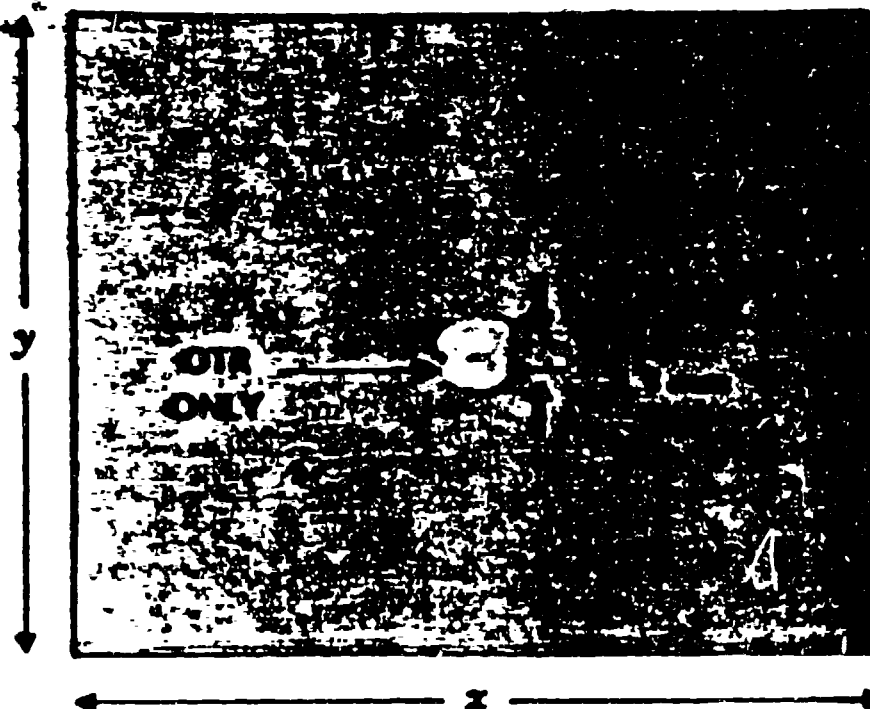


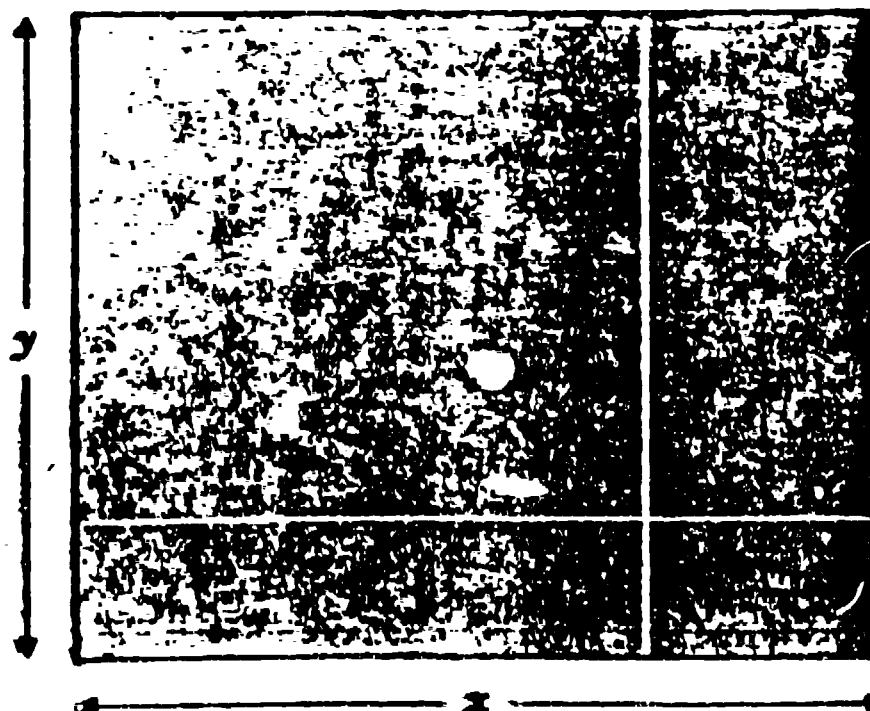
Fig. 15

REFERENCE SCREEN ASSEMBLY PRODUCES BEAMSPOT "DOUBLET"
 IN IMAGE FOR WELL FOCUSED BEAM AT A-leg
 ($E_B = 309 \text{ MeV}$)



FUSED SILICA PLUS
 Al MIRROR ASSEMBLY

(CHERENKOV
 PLUS OTR)



Al MIRROR ONLY

(OTR)

Fig. 16

QTR INTERFEROMETER IMAGE
PROVIDES DIVERGENCE AND ENERGY INFORMATION
(Burst 9/30/89)

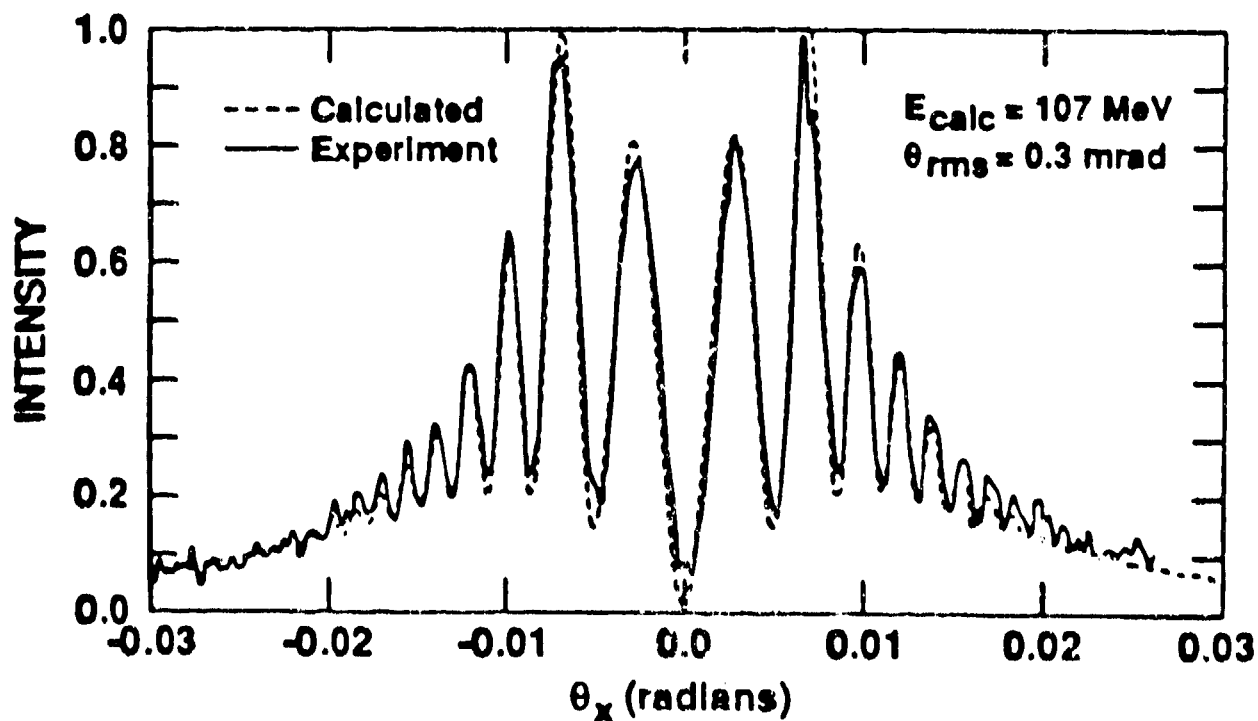
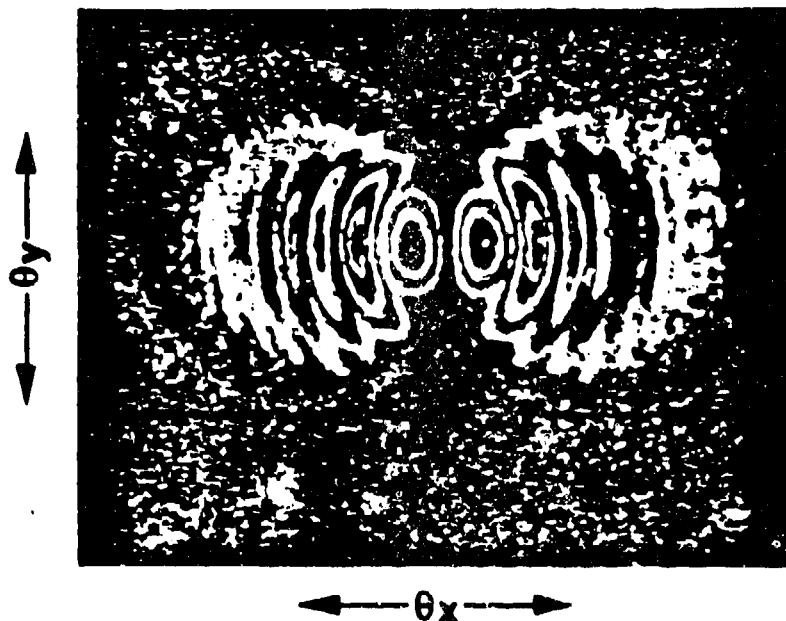
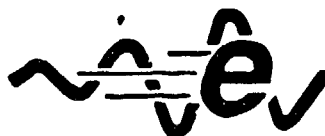


Fig. 17

INNER FRINGES SHOW ELECTRON-BEAM ENERGY EFFECT

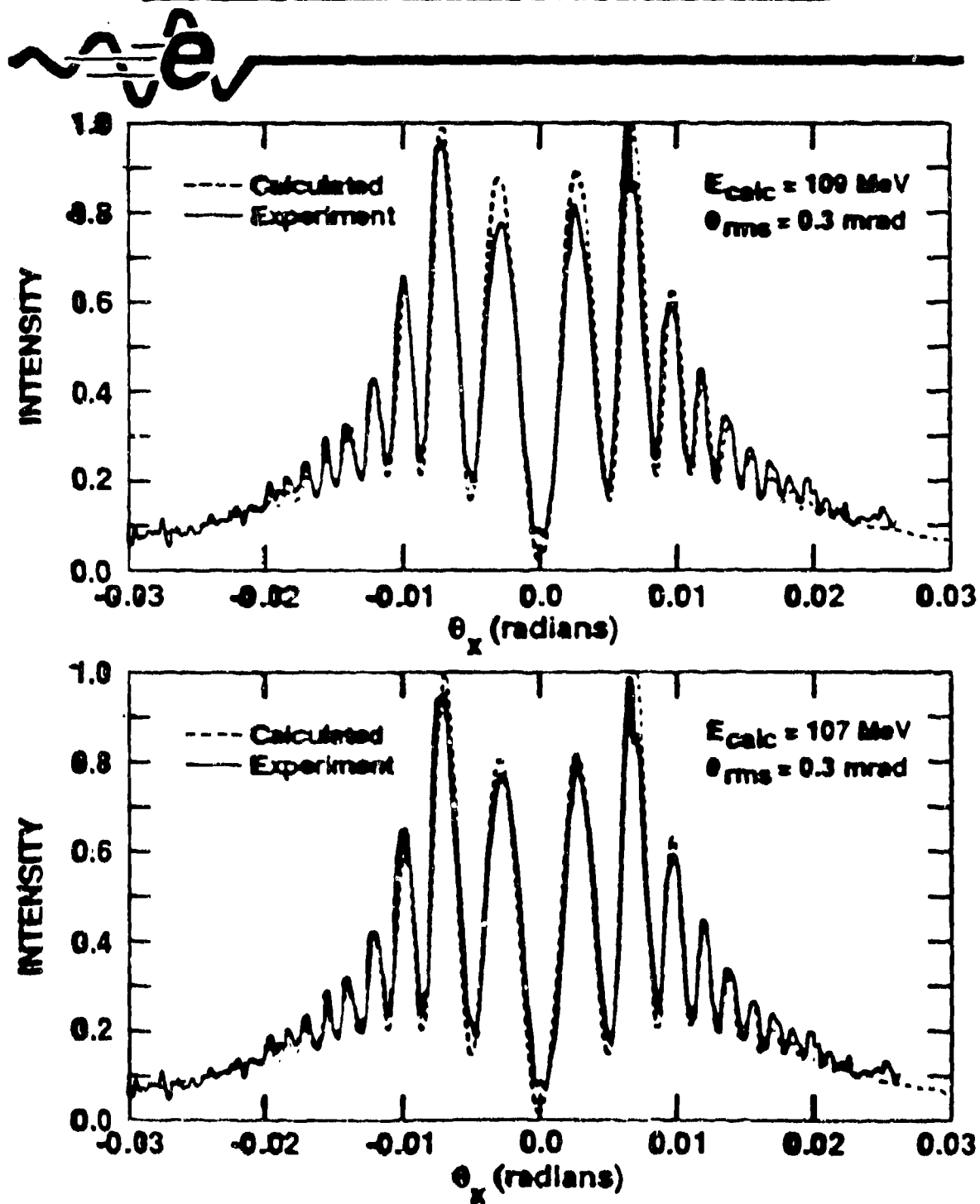
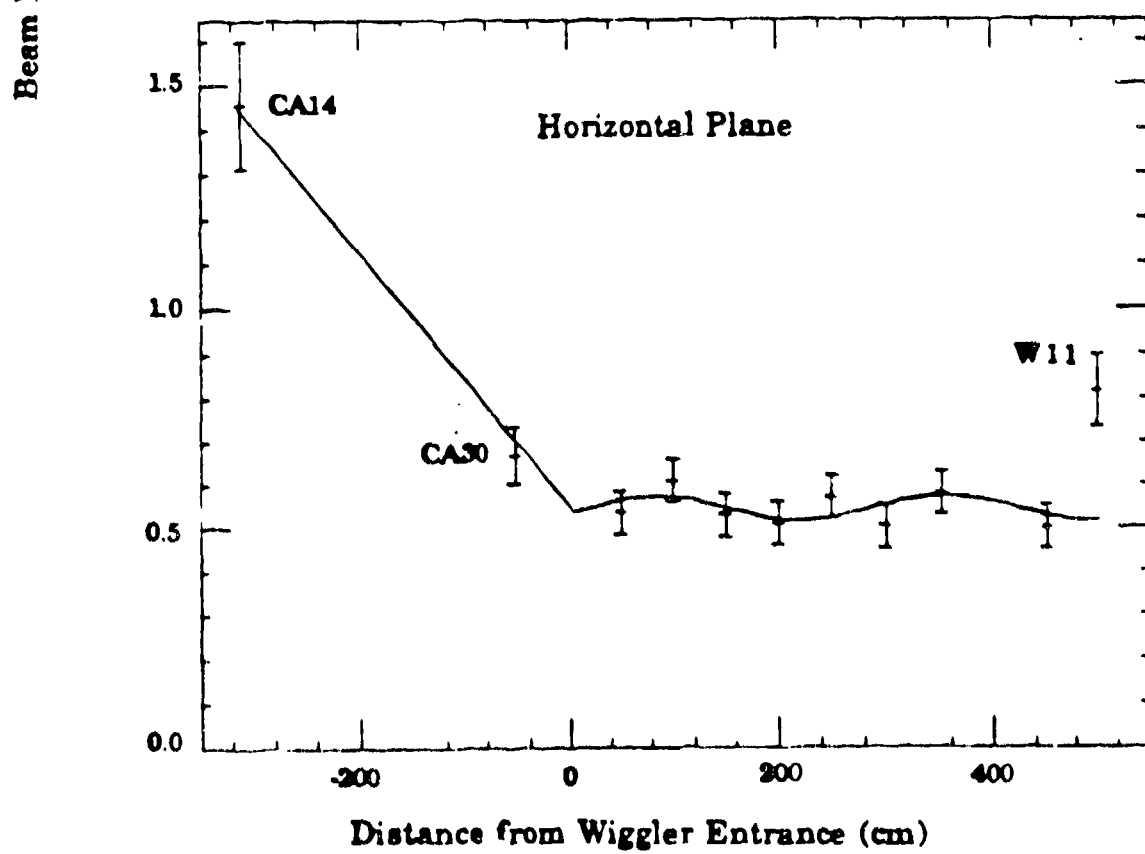
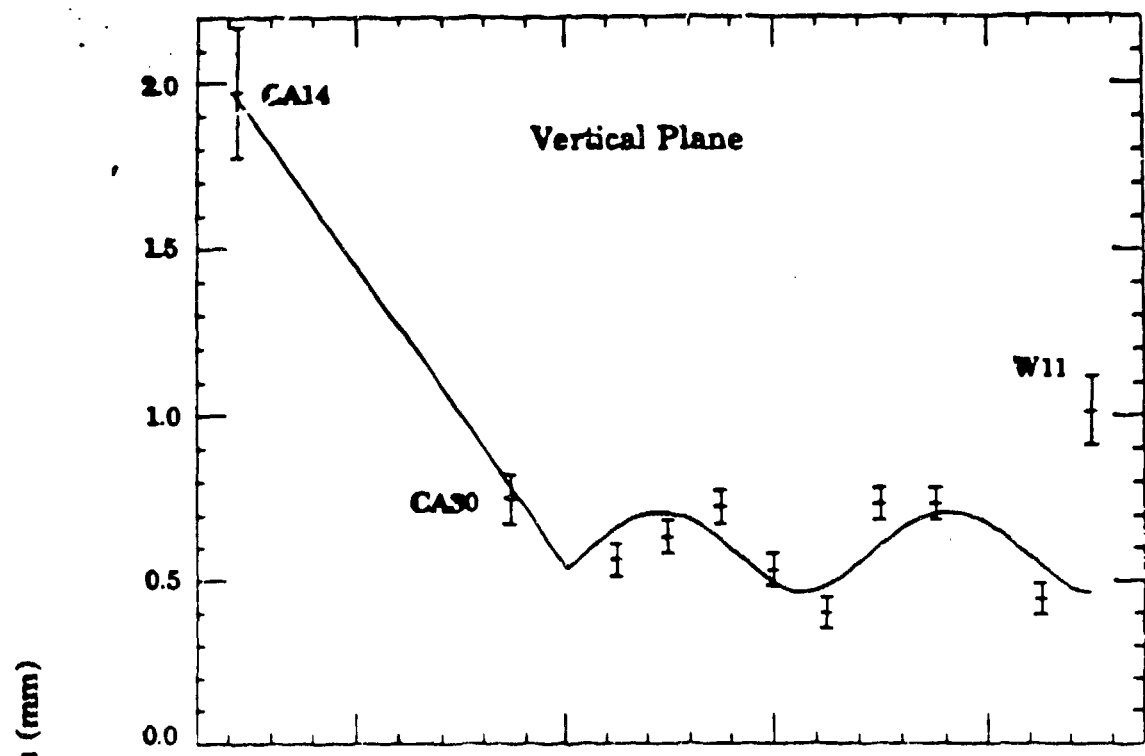
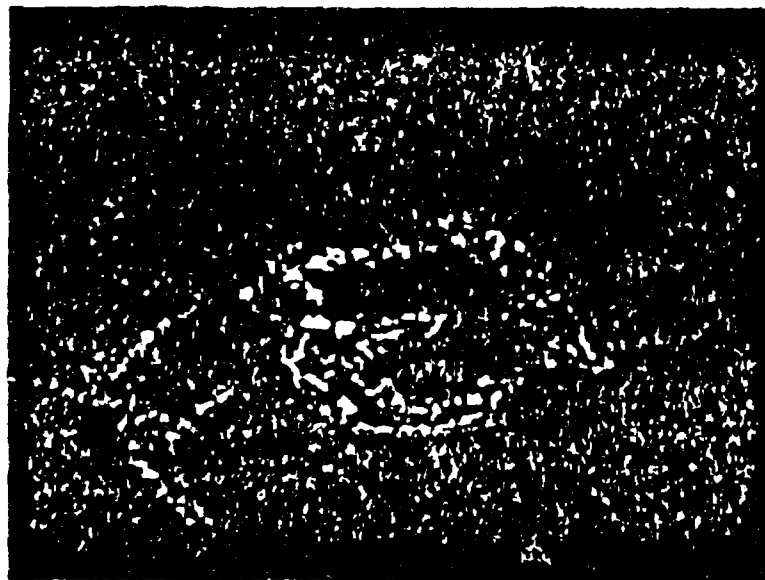


Fig. 18



Electron Beam Matching to Wiggler

ELECTRONS MAKE AN "FEL"

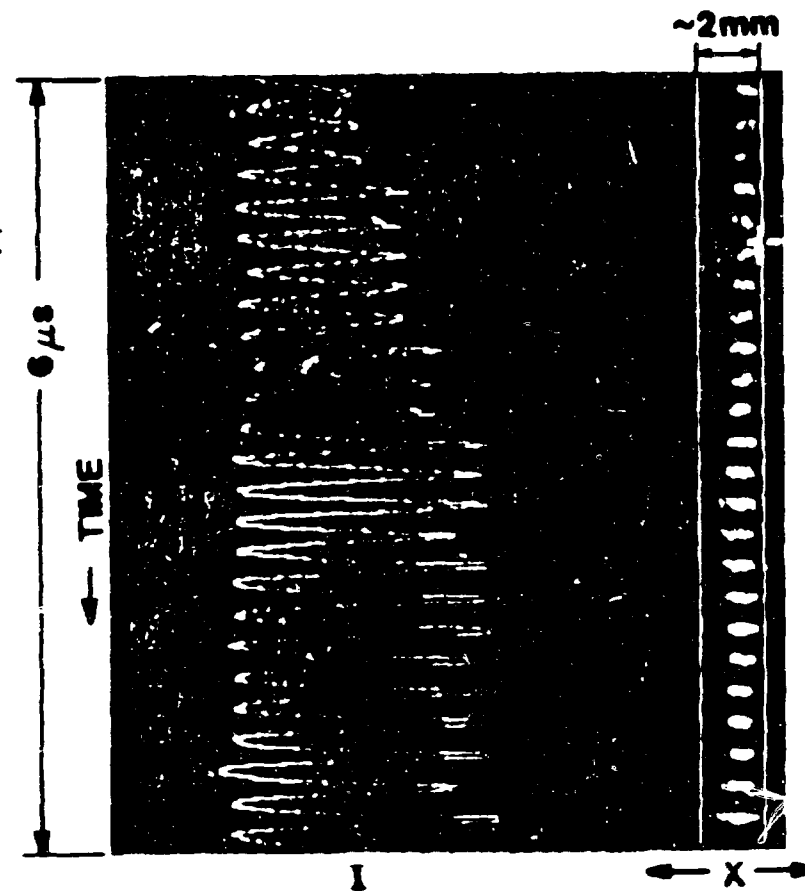


**Electron image 7 m from photocathode
17 MeV**

Fig. 19b

**SPONTANEOUS EMISSION PROVIDES A
NON-INTERCEPTING E-BEAM DIAGNOSTIC IN
WIGGLER REGION USING STREAK CAMERA.**

- SPATIAL PROFILE AND POSITION (x,y)
- INTENSITY PROPORTIONAL TO CHARGE
- MICROPULSE DURATION
- ELECTRON BEAM ENERGY EFFECTS
(streak/spectrometer)



**Example: 20 MACROPULSE AVERAGE
SPONTANEOUS EMISSION $x(t)$**

SYNCHROSCAN STREAK PROVIDES BUNCHING DIAGNOSTIC FROM OUTCOUPLED SPONTANEOUS RADIATION (MACROPULSE)

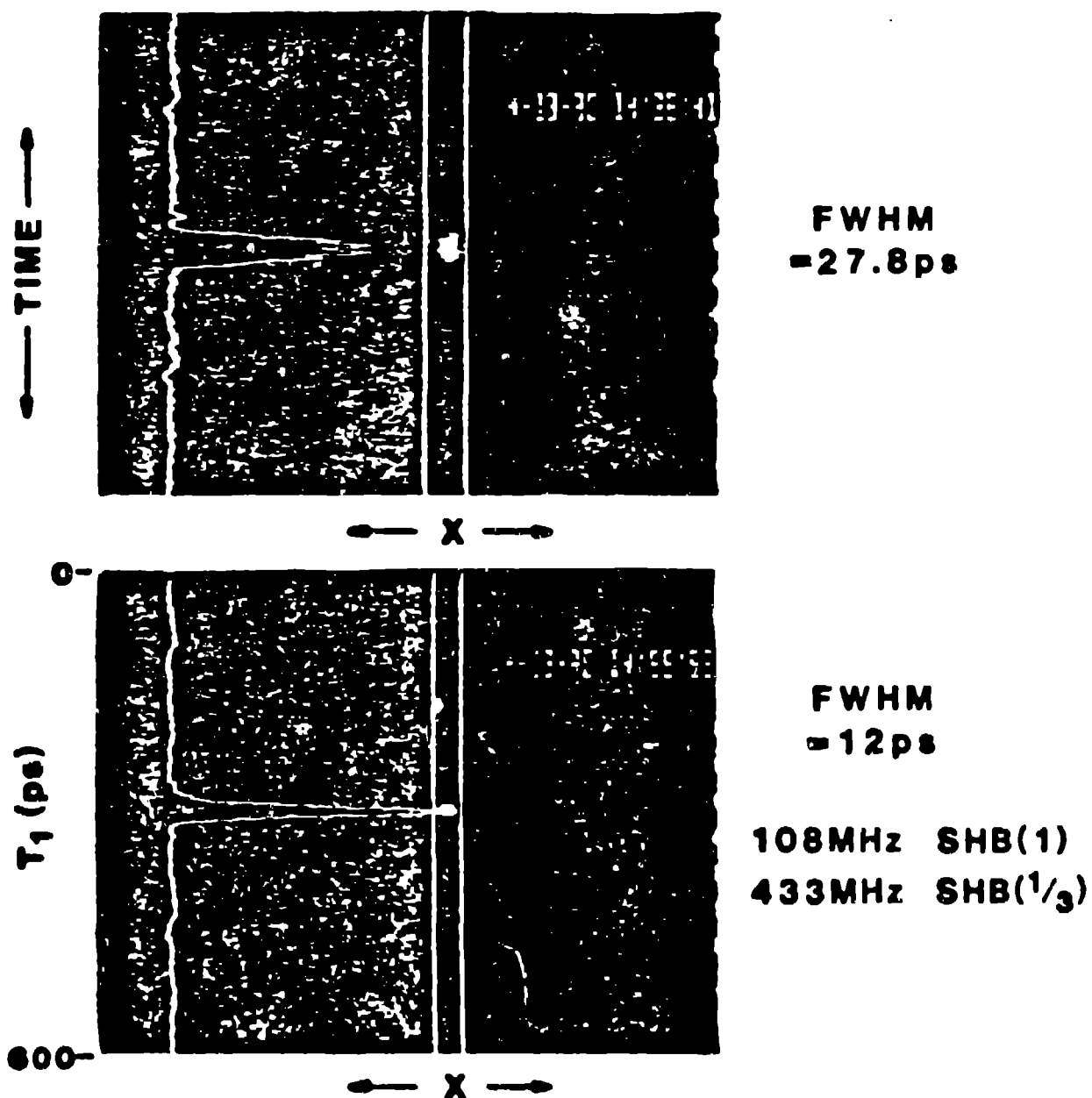
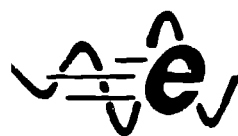


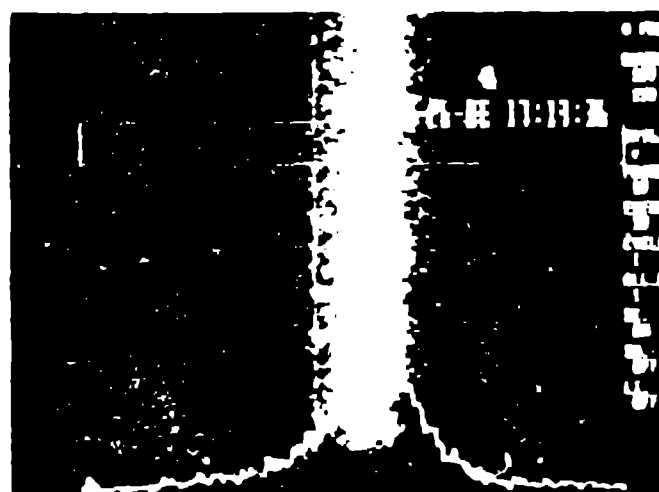
Fig. 21

Electron Beam Energy and Spread Revealed in Spontaneous Emission Spectrum



SPONTANEOUS
EMISSION
(30-macropulse)
average

← TIME

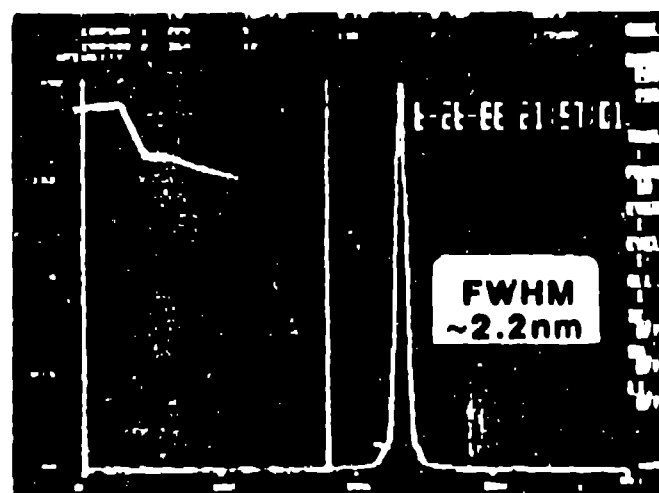


63 μs

← λ

HeNe
REFERENCE

INTENSITY



FWHM
~2.2 nm

← λ

Fig. 22

Spontaneous Emission Spectrum Shifts in Macropulse ($\sim 2\text{nm}$ in last $30\mu\text{s}$)

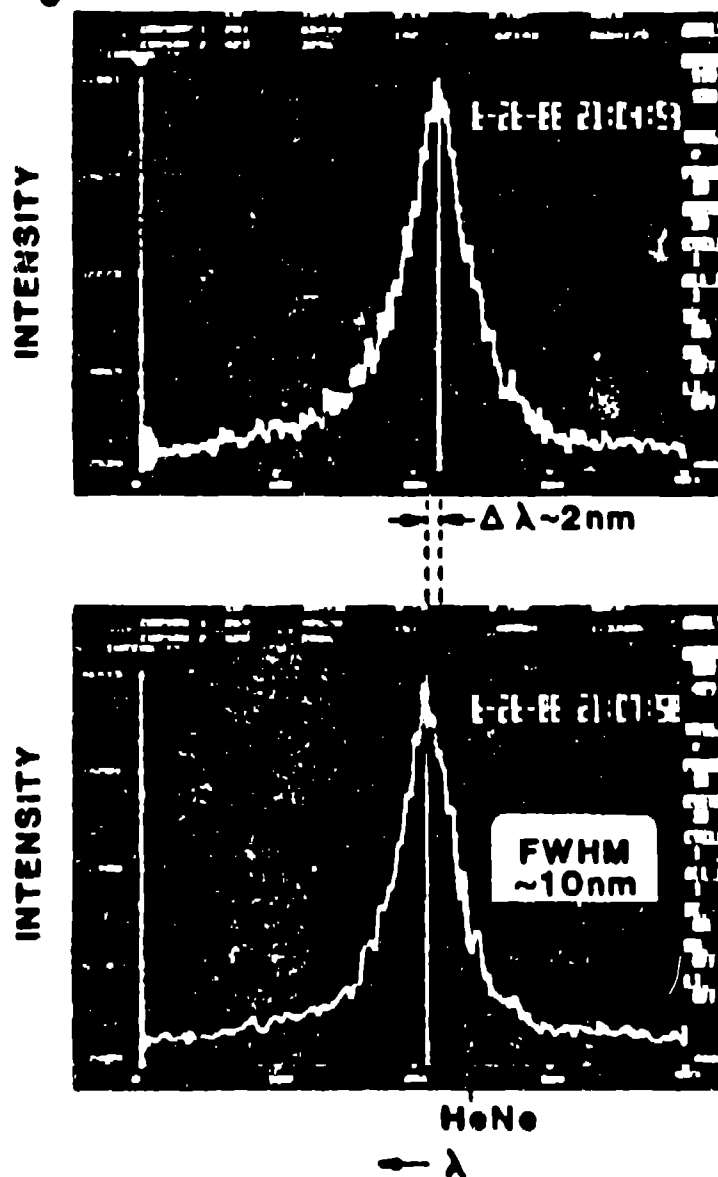
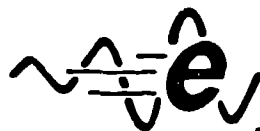


Fig. 23

SPECTRAL EFFECTS OBSERVABLE ON A SINGLE MICROPULSE (< 10ps)

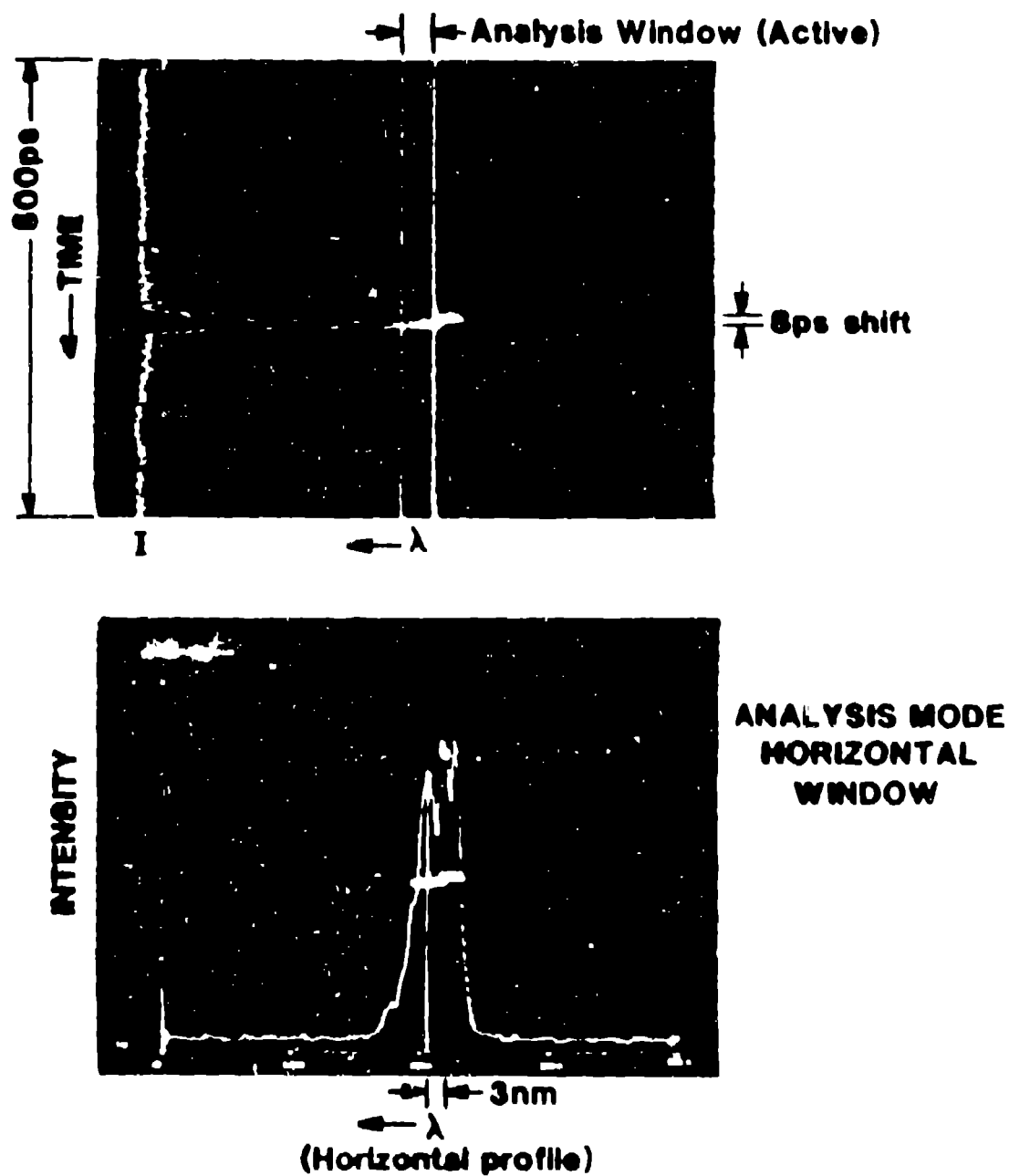


Fig. 24

**TIME-RESOLVED OPTICAL SPECTRA FOR DIFFERENT
CAVITY LENGTH TUNING SHOWING THE SUPPRESSION
OF THE LONGER WAVELENGTH WITH DETUNING**

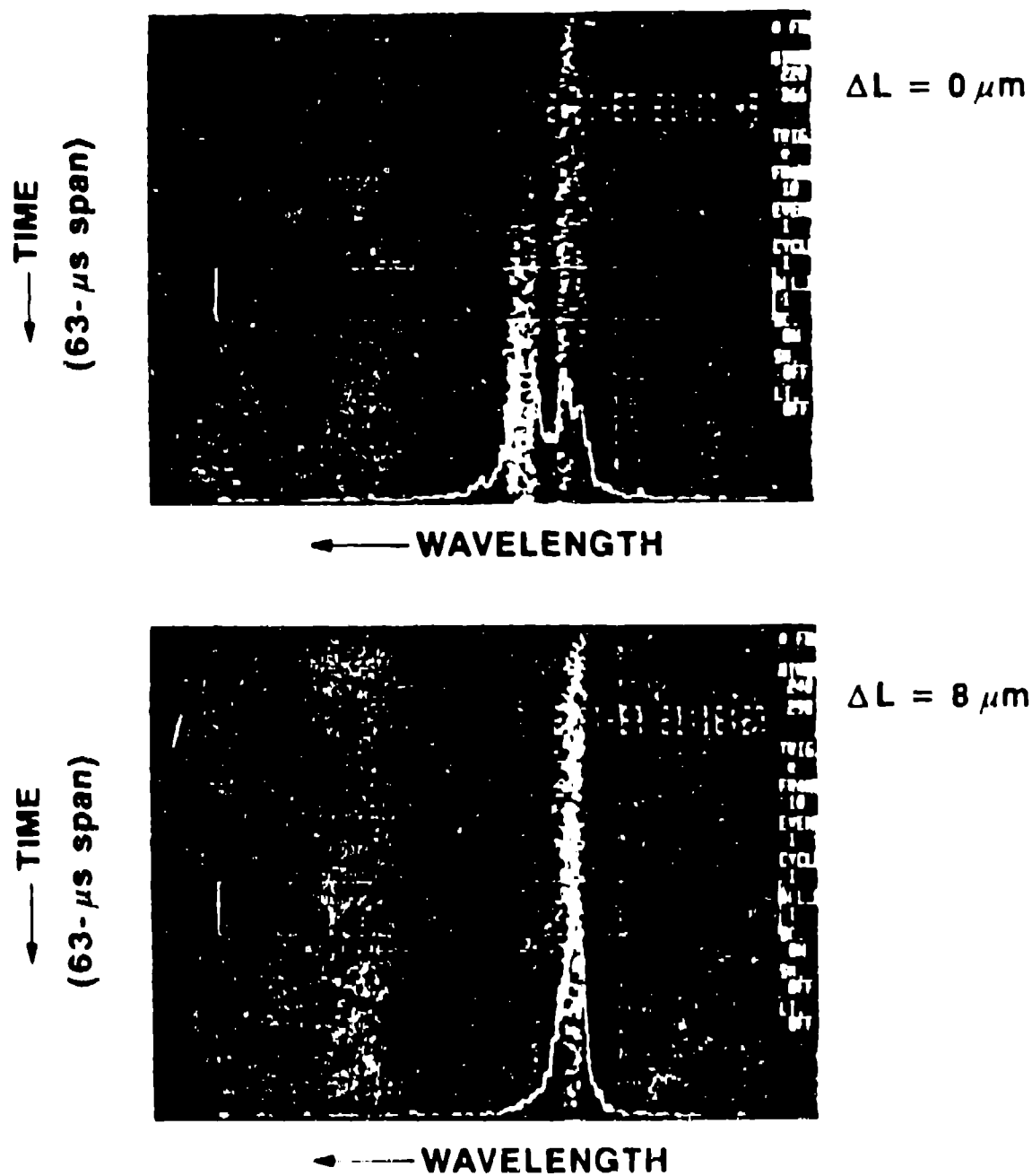


Fig. 25

**CHARACTERISTICS DEPENDENT UPON
PHYSICS OF E-BEAM IN THE FIRST
ACCELERATING CAVITY: CRITICAL FOR
INEX VALIDATION AND ENHANCEMENT**

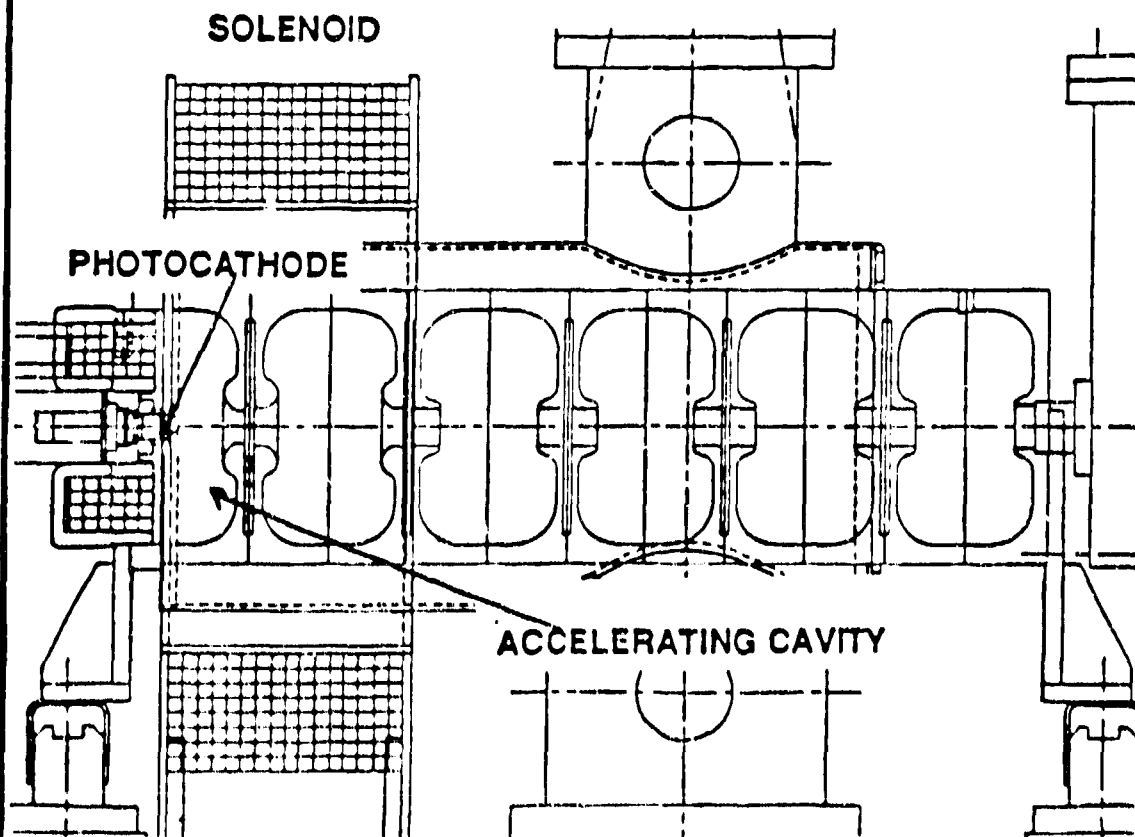


Fig. 26

SIMULTANEOUS SYNCHROSCAN STREAK OF E-BEAM/DRIVE LASER (DL) (D. L. PHASE EFFECT)

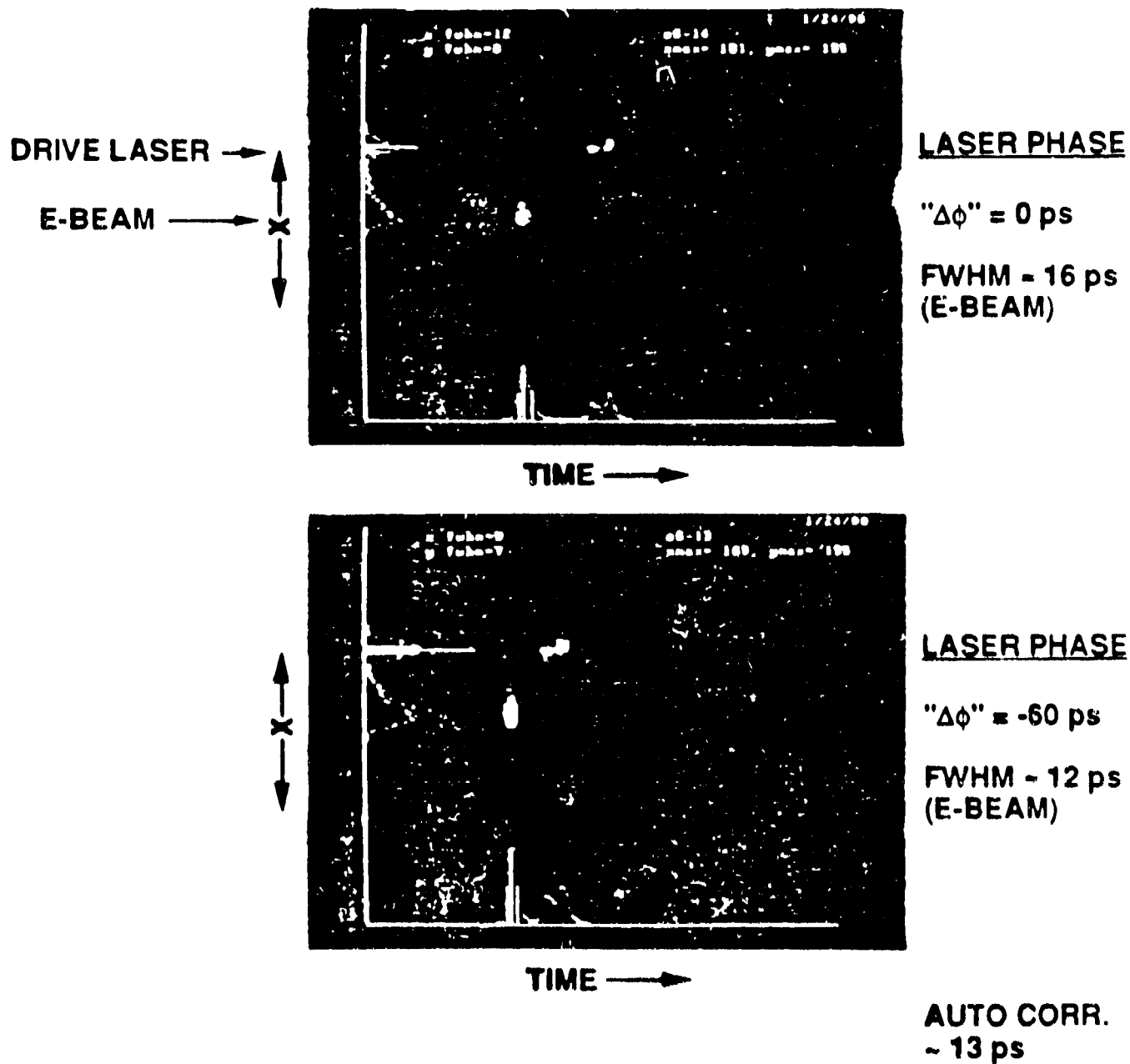


Fig. 27

**MEASURED μ PULSE LENGTH VARIATION
WITH LASER PHASE IN INJECTOR
AGREES WITH INEX PREDICTION**

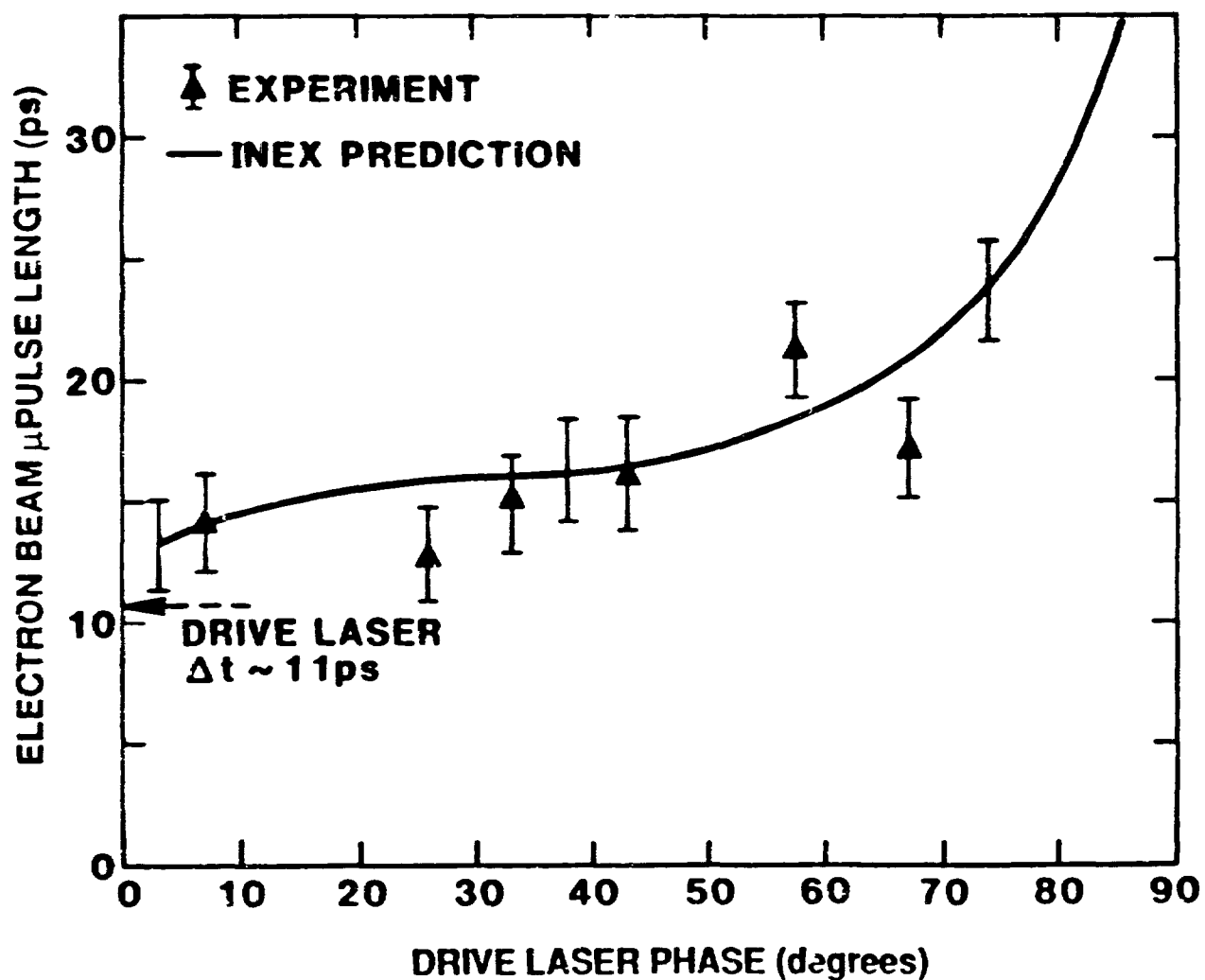


Fig. 28

**MEASURED ELECTRON-TRANSIT-TIME
VARIATION WITH LASER PHASE IN
INJECTOR AGREES WITH
INEX PREDICTION**

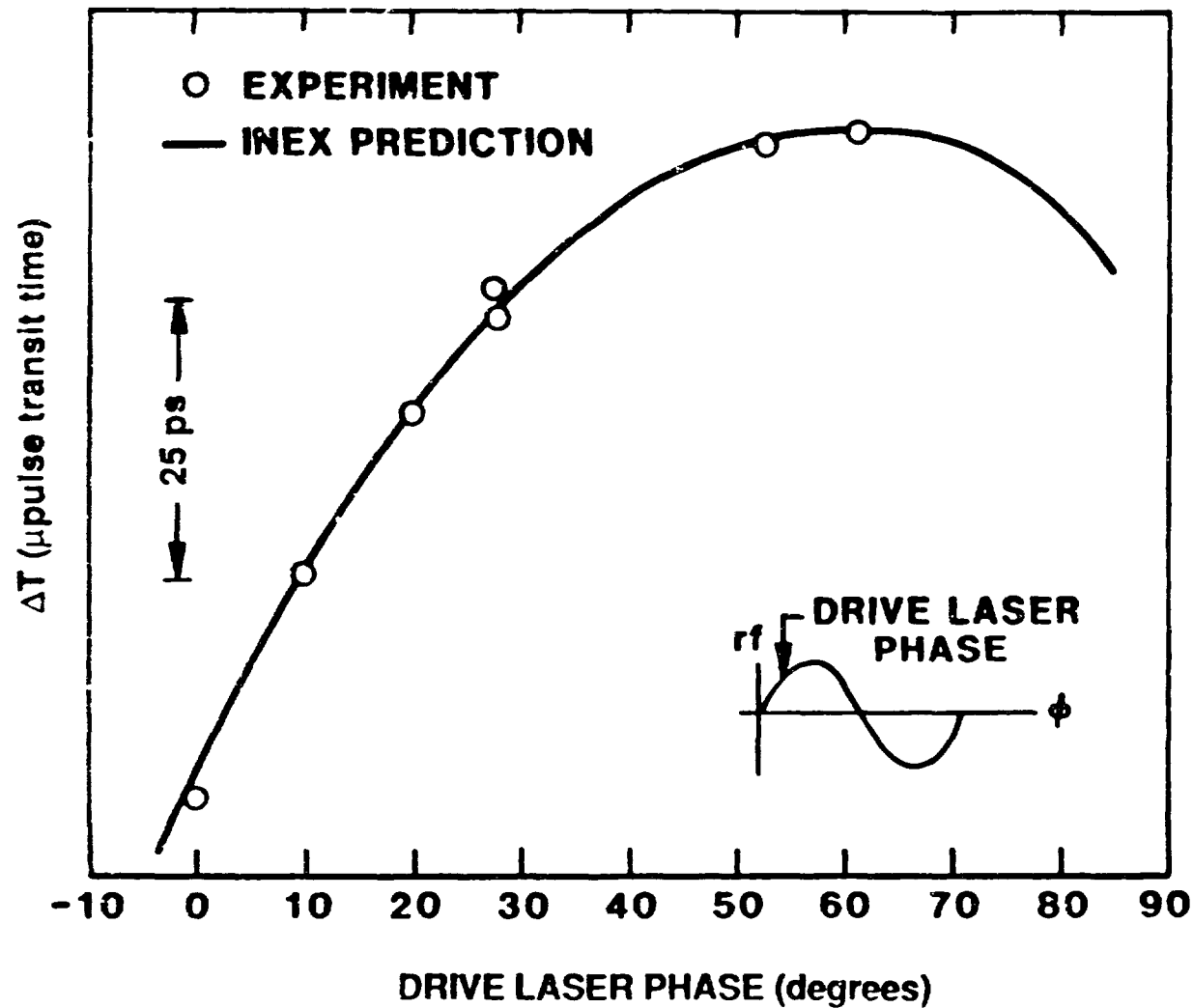


Fig. 29

SYNCHROSCAN STREAK PROFILES
TRACK DRIVE - LASER PHASE JITTER (3-13-90)

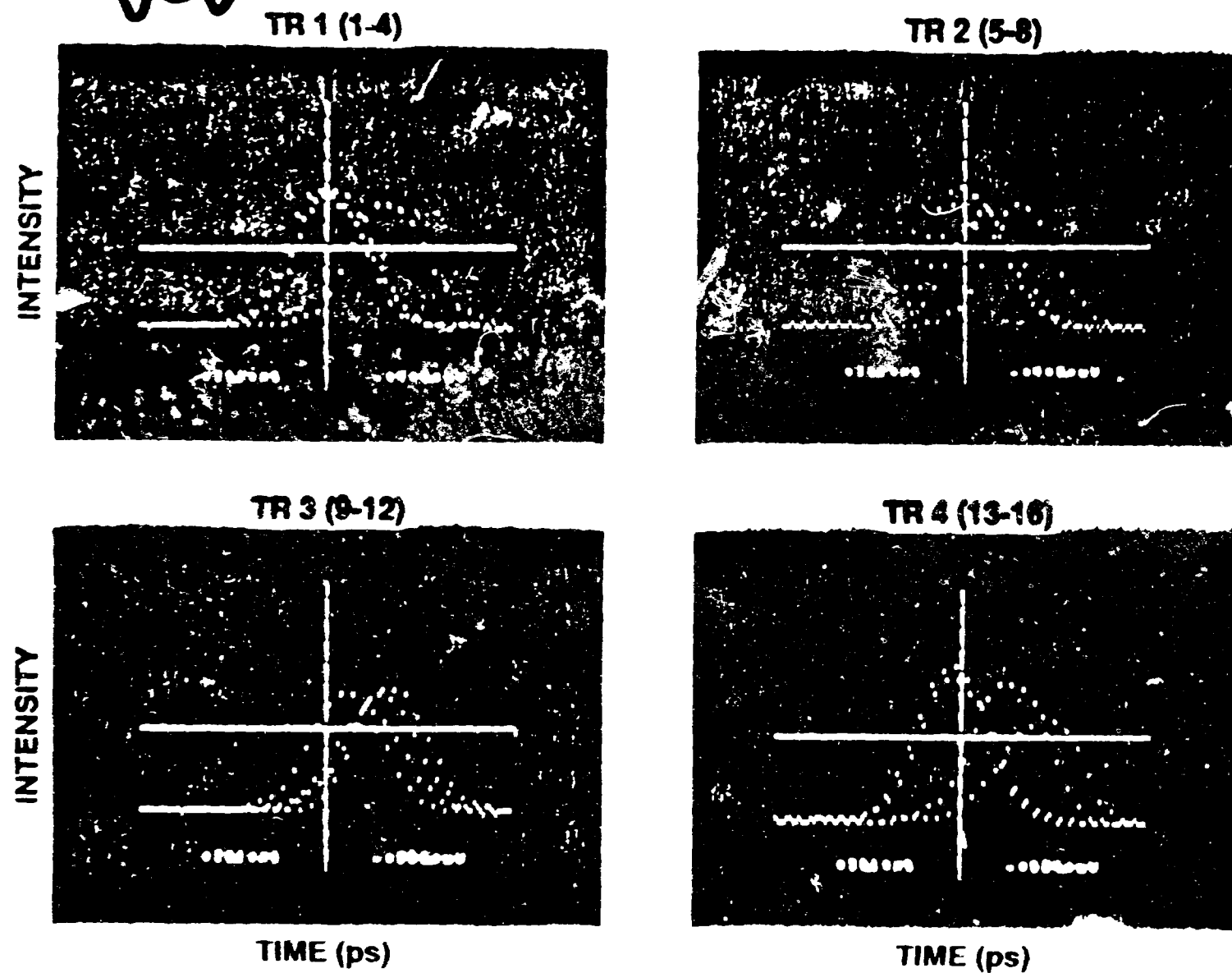


Fig. 30

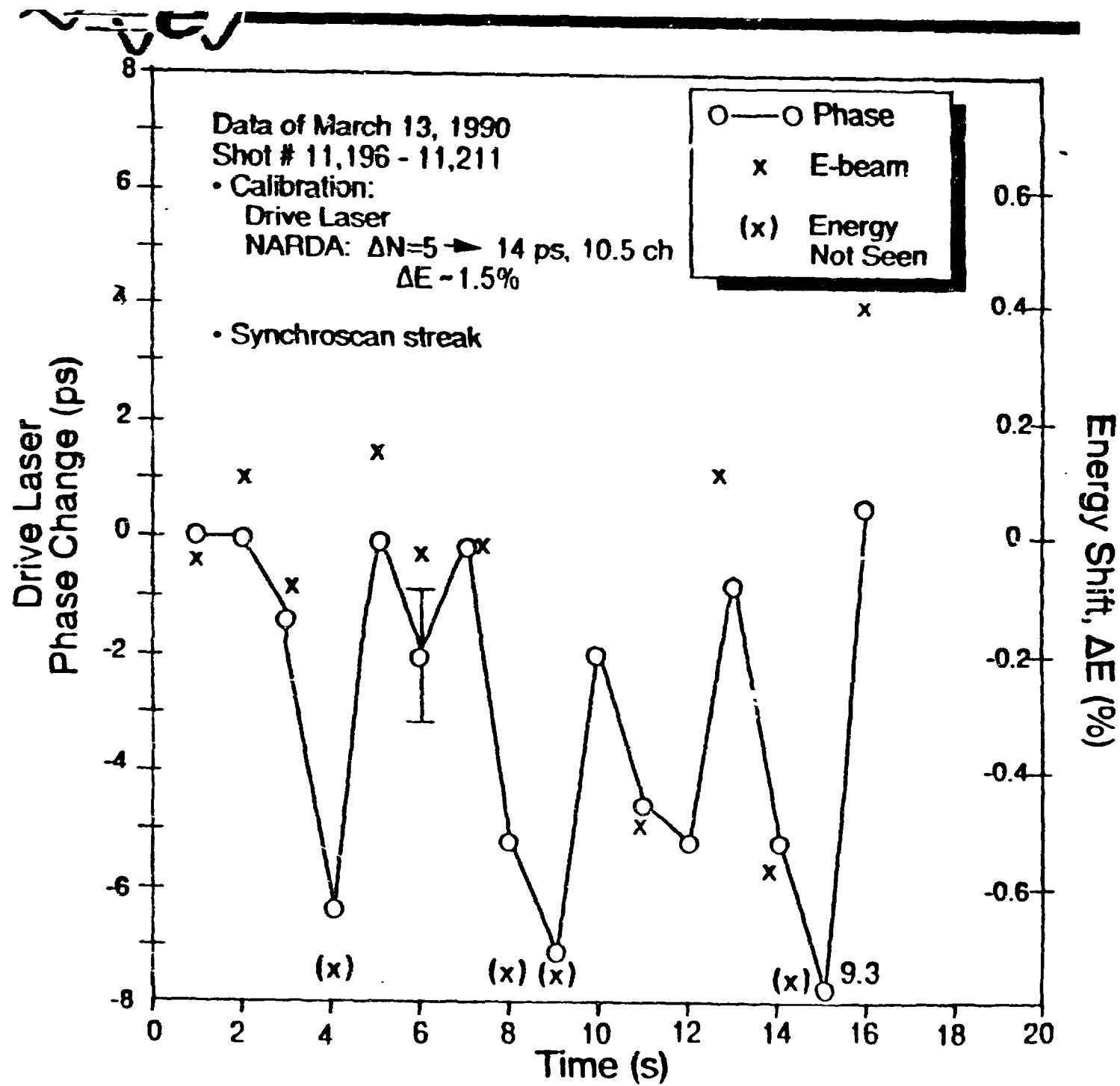


Fig. 31

**DRAMATIC IMPROVEMENTS IN DRIVE LASER PHASE
STABILITY HAVE BEEN DEMONSTRATED
(HIBAF, APRIL 1990)**

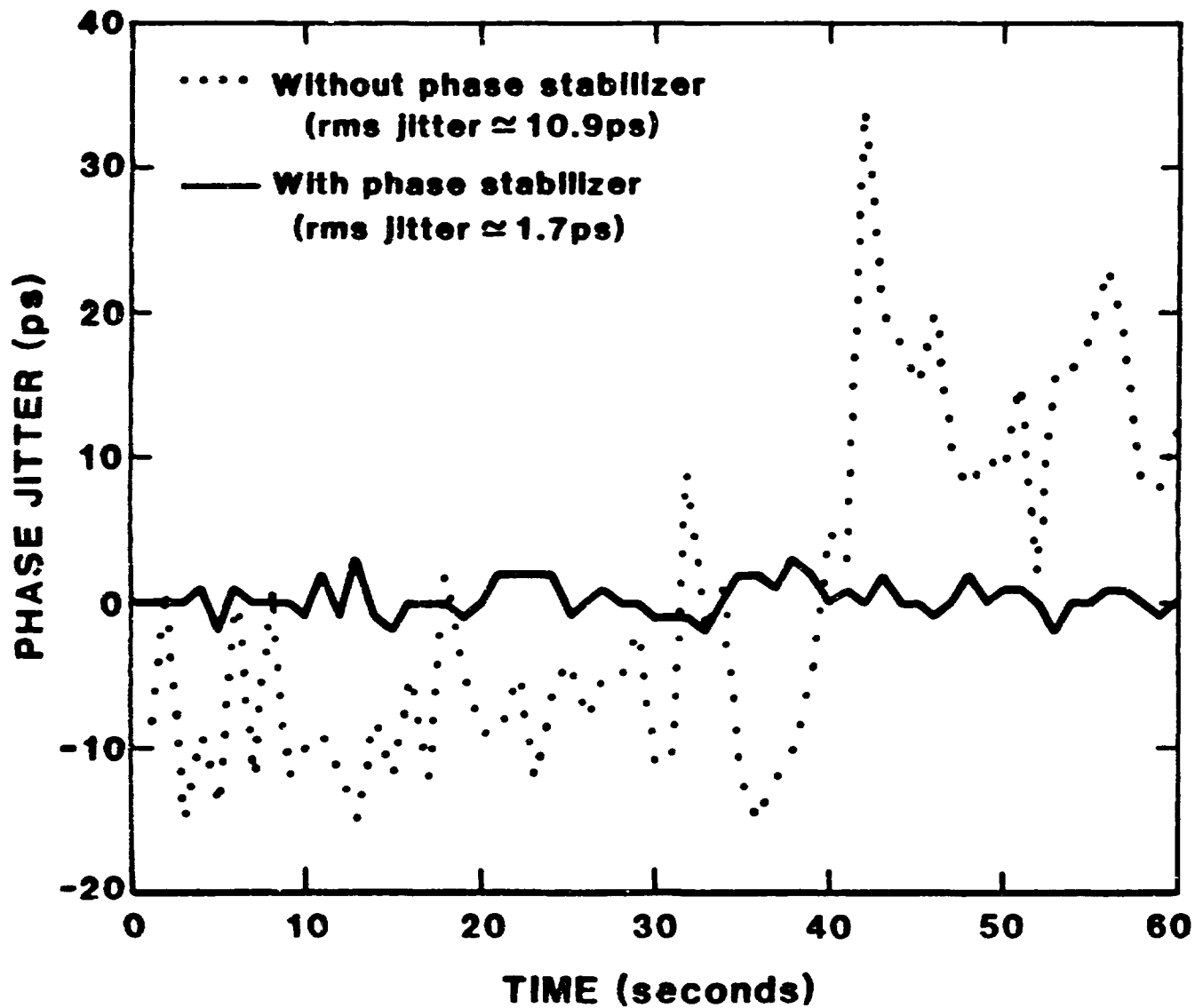
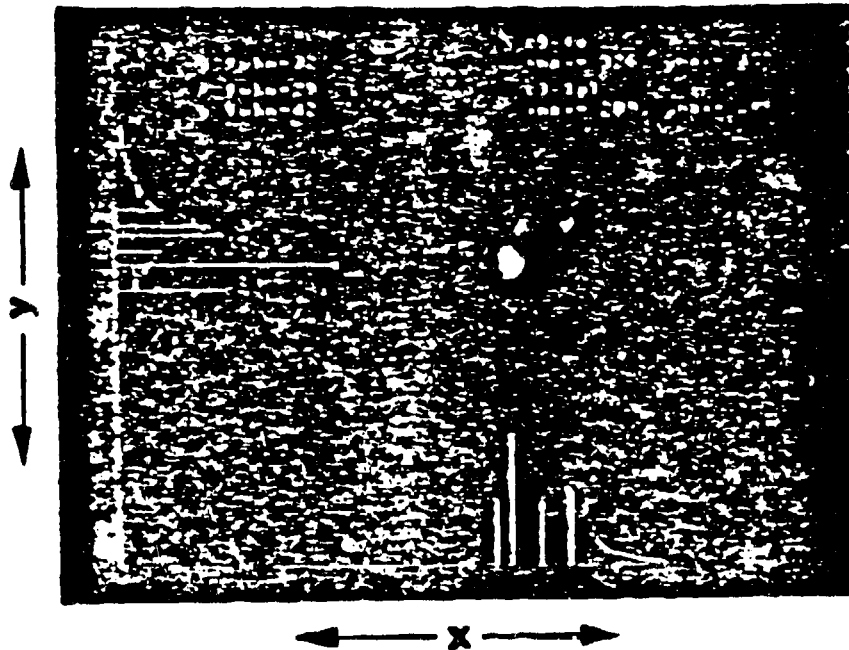
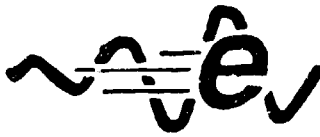
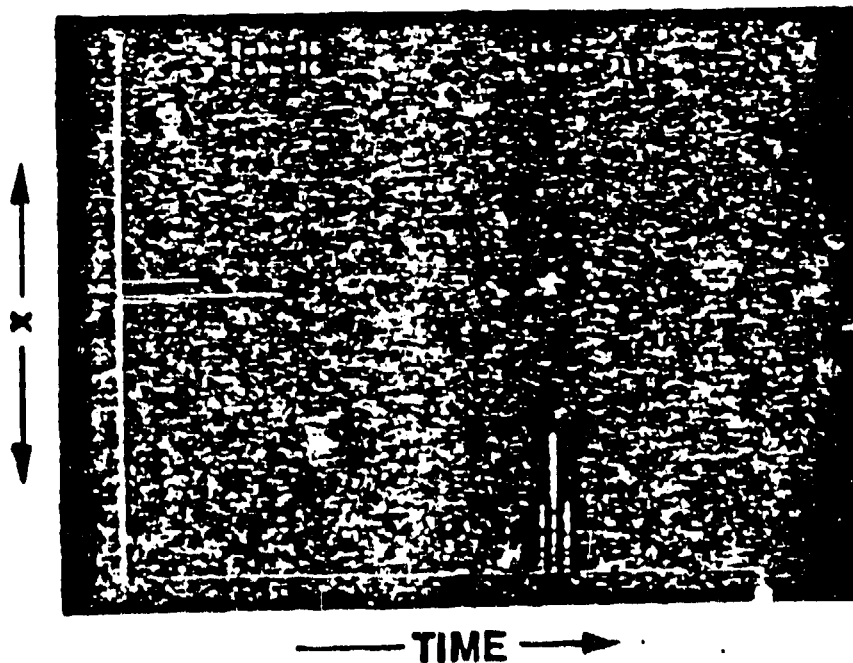


Fig. 32

FIELD EMISSION ELECTRONS
COMPARABLE TO SINGLE MICROPULSE
(3-15-90)



BEAMSPOTS
 - Field Emission
 - Single μ Pulse



Synchroscan
Streak of
Field Emission
Electrons Only
 $\Delta t \sim 20$ ps

Fig. 33

INITIAL DUAL SWEEP STREAK IMAGES PROVIDE SIMULTANEOUS MICROPULSE AND MACROPULSE INFORMATION

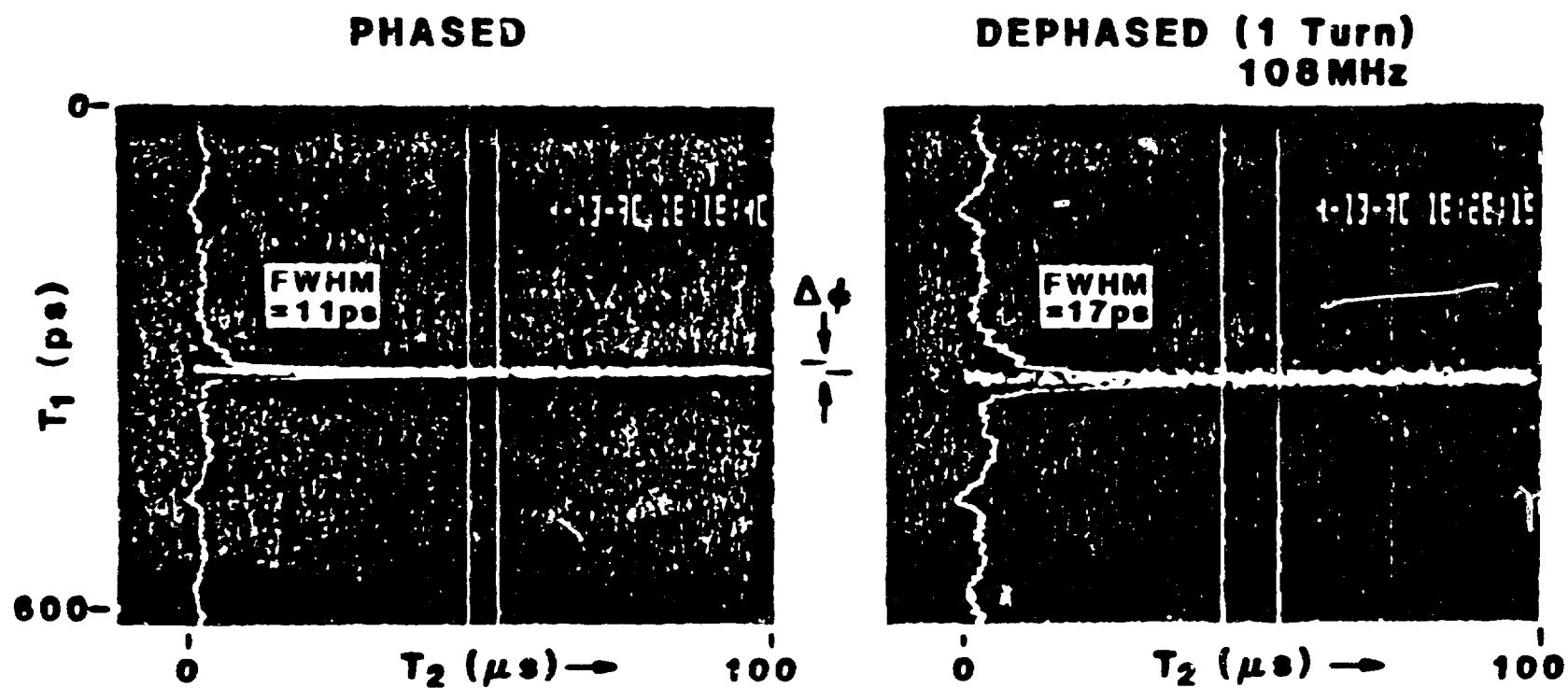


Fig. 34

DUAL SWEEP STREAK IMAGE DISPLAYS BOTH MACRO AND MICROPULSE LASING EFFECTS (MAY, 1990)

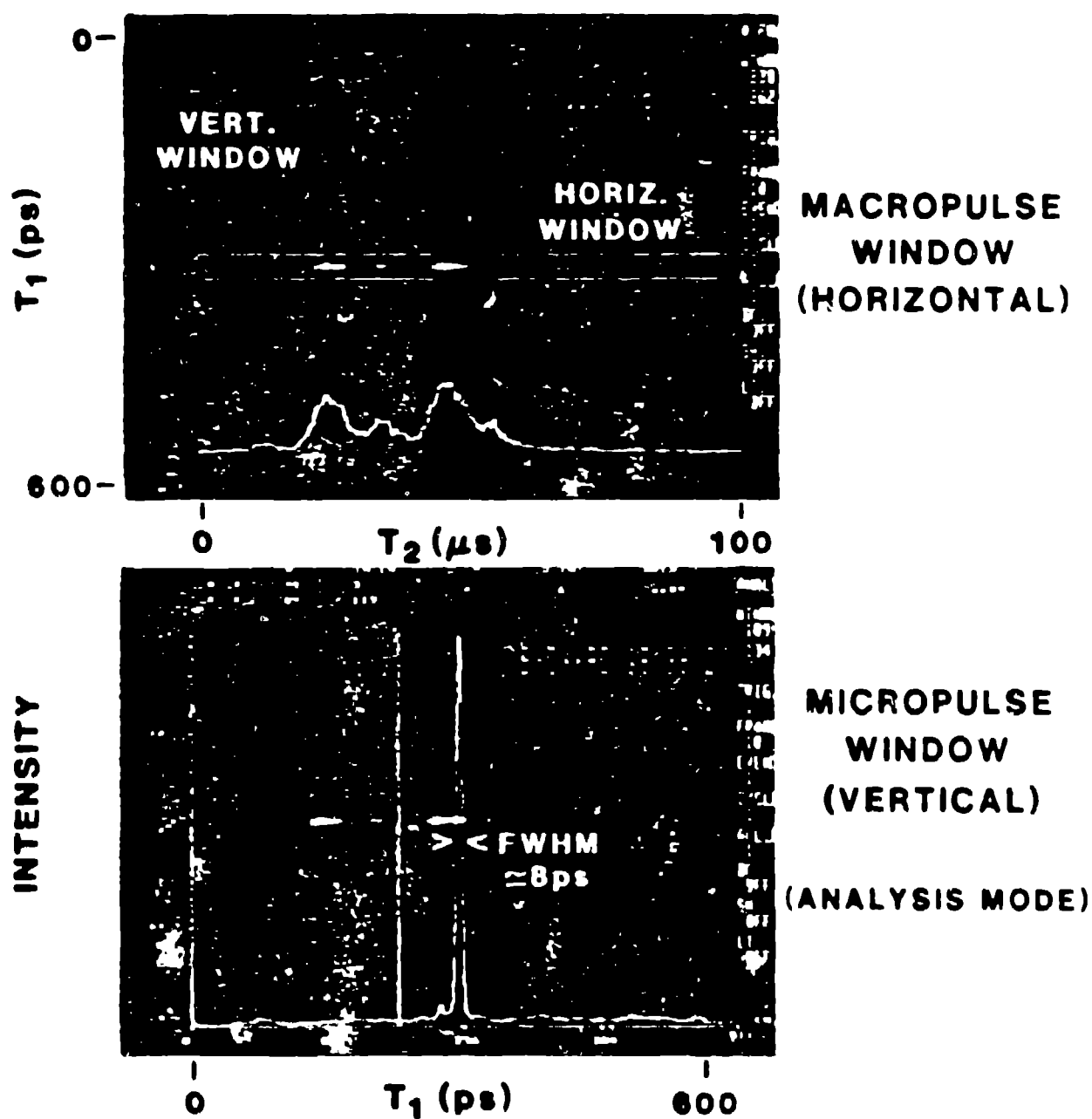


Fig. 35